MISSIONE 4
ISTRUZIONE RICERCA

National Recovery and Resilience Plan (NRRP)

Mission 4, Component 2 (M4C2) – Investment 1.1: Fund for the National Research Programme (NRP) and Research Projects of Significant National Relevance (PRIN)

Call PRIN 2022 PNRR – Directorial Decree no.1409, 14/09/2022

SubRISK+

Enhancing our understanding of Subsidence RISK induced by groundwater exploitation towards sustainable urban development

CUP: B53D23033400001

DEL 4.3

Numerical modelling on hydrodynamics and land subsidence coupling with Bayesian-based data assimilation, the Bologna case study

Authors: X. Tang, P. Teatini, C. Zoccarato (UNIPD), R. Bonì (IUSS), F. Cigna, R. Paranunzio (CNR-ISAC)

Version 1.0, Issue date: 28/02/2026

Dissemination level: Public

Finanziato dall'Unione europea NextGenerationEU | Ministero dell'Università e della Ricerca | Italiadomani | CNR ISAC | IUSS Scuola Universitaria Superiore Pavia | Università degli Studi di Padova

How to cite this document

TANG X., TEATINI P., ZOCCARATO C., BONÌ R., CIGNA F. & PARANUNZIO R. (2026). *PRIN 2022 PNRR SubRISK+ Deliverable DEL 4.3: Numerical modelling on hydrodynamics and land subsidence coupling with Bayesian-based data assimilation, the Bologna case study*, Version 1.0, Issue date: 28/02/2026, pp. 52. Public Report. Available at: https://www.subrisk.eu/deliverables

Acknowledgements

The authors would like to thank Dr. Andrea Chahoud, Dr. Marco Marcaccio and Dr. Marianna Mazzei of the ARPAE Emilia-Romagna, Dr. Paolo Severi, Dr. Luisa Perini and Dr. Lorenzo Calabrese of the Regione Emilia-Romagna for the provided datasets and fruitful discussions about the project outcomes.

Revision history

Revision no.	*Authors*	*Date*	*Description*
1.0	TANG X, TEATINI P., ZOCCARATO C., BONÌ R., CIGNA F., & PARANUNZIO R.	28/02/2026	First release

Executive summary

This report summarizes the results of SubRISK+ Work Package (WP) n.4 (*WP4: Advanced Local Scale Modelling*). WP4 is aimed to 1) develop city-scale representative lithofacies model reflecting the high heterogeneity and uncertainty of o the aquifer system, 2) integrate the lithofacies model into a 3D fluid-dynamic model coupled with a 3D geomechanical model, 3) simulate land subsidence (and horizontal displacements) by the comprehensive modelling system, and 4) perform EO data assimilation with the aim to improve its capacity for land subsidence prediction over the next decades. The advanced modelling system is developed for the city of Bologna and its suburban area, the Italian metropolitan city where land subsidence has reached the highest values, up to 3.5 m over the period from 1900 to 2020 (Zuccarini et al., 2024), forcing regional and local authorities to take legislative measures aimed to control the process (law, 10 December 1980, n. 845). The subsidence rate is also today larger than 20 mm/year in some portions of the city (https://egms.land.copernicus.eu/).

The state-of-the-art modelling approach proposed in this study is aimed to account for the peculiarity of the Bologna case study and to respond to the SubRISK+ goals: a) the 3D approach, both for the flow and the geomechanical simulations, allows a comprehensive quantification of differential displacements caused by groundwater withdrawal; b) the stochastic approach, both in terms of hydrogeological setting and parameters estimation, allows to account for the uncertainties related to the subsurface features of the Bologna metropolitan area in the modelling framework.

This DEL4.3 describes the modelling strategy implemented to simulate the piezometric evolution in the heterogeneous aquifer system of Bologna and the following 3D displacement field. The simulations have been carried out by means of two state-of-the-art finite element simulators developed at UNIPD. The uncertainty of the hydro-geomechanical parameters, specifically the hydraulic conductivity and soil compressibility, has been reduced by assimilating yearly piezometric measurements recorded from 1976 to 2021 and InSAR land subsidence rates from 1992 to 2021. The model simulations have been extended to 2050 and 2100, investigating the expected evolution of the quantities of interest in relation to the RCP4.5 and RCP8.5 climatic scenarios.

Contents

1. INTRODUCTION

SubRISK+: Enhancing our understanding of Subsidence RISK induced by groundwater exploitation towards sustainable urban development is a collaborative two years research project funded in 2023-2026 in the framework of the Italian National Recovery and Resilience Plan (NRRP), Mission 4, Component 2 (M4C2) – Investment 1.1: Fund for the National Research Programme (NRP) and Research Projects of Significant National Relevance (PRIN) [Call "PRIN 2022 PNRR", D.D. no.1409, 14/09/2022], and led by the National Research Council (CNR) of Italy – Institute of Atmospheric Sciences and Climate (ISAC), in collaboration with the University School for Advanced Studies (IUSS) of Pavia – Department of Science, Technology and Society (STS), and the University of Padua (UNIPD) – Department of Civil, Environmental and Architectural Engineering (ICEA).

With reference to the city of Bologna, which has been selected as local hotspot for the SubRISK+ analyses at the local scale, this report (DEL4.3) provides the results of SubRISK+ Work Package (WP) n.4 (*WP4: advanced local scale modelling*), aimed to i) characterize through a Bayesian-based approach the evolution of the pore pressure in the heterogeneous aquifer system of Bologna, which has been deeply exploited since the 1950s to supply water to inhabitants and industrial activities of the city, ii) characterize through a Bayesian-based approach the evolution of the displacement field (land subsidence and horizontal components) of the land surface at Bologna study area resulting from the pressure change in the aquifer system; and c) forecast the future evolution of the displacement fields to 2025 and 2100 accounting for climatic scenarios (RCP4.5 and RCP8.5) and the expected evolution of the urban pressure.

The goal is also achieve the specific project aims listed above through a novel modelling framework, which integrates heterogeneous lithofacies characterization of the aquifer system into a 3D finite element grid used for fluid-dynamic and geomechanical simulations, with the use of an ES-MDA (Ensemble Smoother with Multiple Data Assimilation) algorithm to reduce the uncertainty associated to the key hydro-geomechanical properties of the aquifer facies.

The activities reported in this deliverable take advantage of the outcomes provided in DEL2.2 and DEL3.3 (in terms of land subsidence measured by InSAR in the metropolitan area of Bologna), DEL4.1 (in terms of lithofacies characterization of the Bologna aquifer system), and DEL6.3 (in terms of climatic scenarios and population evolution until 2100).

The digital versions of the output displacement maps in 2050 and 2100 under RCP4.5 and RCP8.5 for the city of Bologna are publicly available through SubRISK+ project website within the '*Control Room*' (https://controlroom.subrisk.eu), which enables open access to SubRISK+ mapping products.

Deliverable 4.3 is structured as follows:

- section 2 describes the data available (section 2.1) and the methodology implemented (section 2.2) to set-up the modelling framework;
- section 3 presents the modelling application to the study area and the results obtained in terms of piezometric evolution and land subsidence until 2021;
- section 4 summarizes the modelling outcome for the prediction scenarios in 2025 and 2100.

2. DATA & METHODS

2.1. Input datasets

2.1.1. General context

The input datasets of the analysis include: (i) geological datasets of the Emilia-Romagna geoportal (https://geoportale.regione.emilia-romagna.it/download), (ii) the hydrogeological data provided by the Regional Agency for Prevention, Environment and Energy of Emilia-Romagna (Arpae), Italy (https://www.arpae.it/it/temi-ambientali/acqua/dati-acque/acque-sotterranee/rete-di-monitoraggio-acque-sotterranee/il-monitoraggio-quantitativo-delle-acque-sotterranee), (iii) the ground displacement observations derived from the Copernicus European Ground Motion Service (EGMS) (https://egms.land.copernicus.eu/), and the regional subsidence monitoring project of Emilia-Romagna region (https://www.arpae.it/it/temi-ambientali/suolo/subsidenza/la-rete-regionale-di-monitoraggio-della-subsidenza), and the (iv) urban settlement information derived from global databases and a dataset provided by the Emilia-Romagna region.

2.1.2. Hydraulic heads from piezometric monitoring wells

The piezometric records for the Bologna study area are available from 52 piezometric monitoring wells, with records spanning the period from 1972 to 2023. Figure 1 shows the spatial distribution of these monitoring wells within the study area. However, not all of these wells monitor the confined aquifer system, as some are screened within the phreatic aquifer. Consequently, only 32 of the 52 monitoring wells, namely those tapping the confined aquifers, are considered suitable for defining the initial and boundary conditions of the numerical model presented in the following section, as shown in Figure 2.

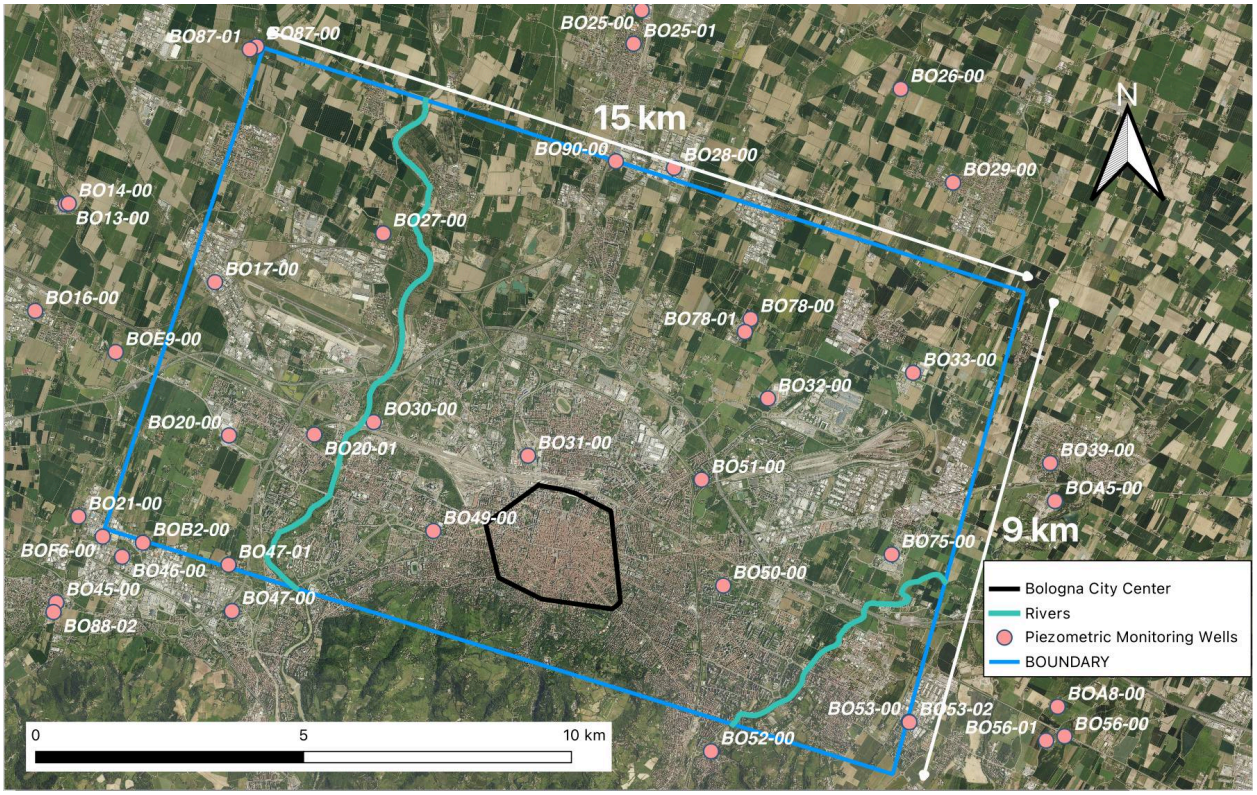

Figure 1 – Location of the piezometric monitoring wells in the study area of Bologna

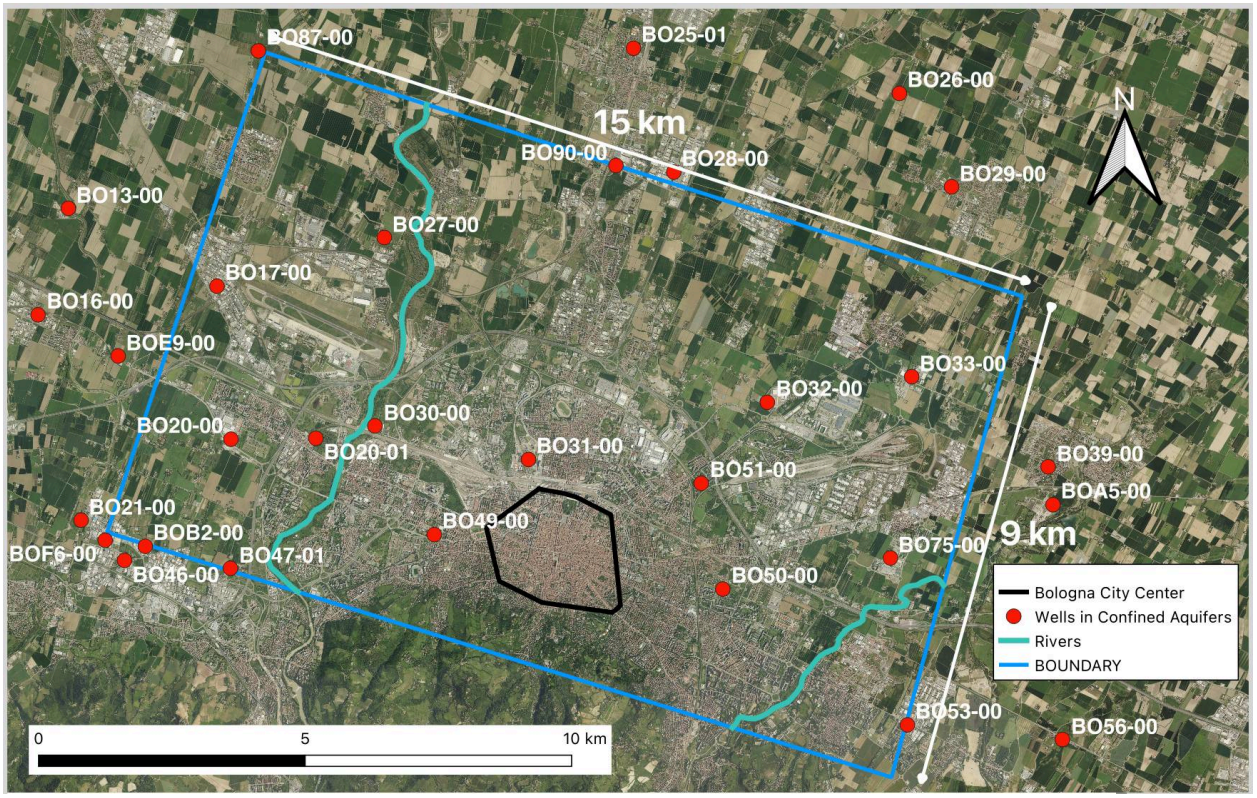

Figure 2 – Location of the piezometric monitoring wells sampling the confined aquifer system

2.1.3. Groundwater withdrawal in Bologna area

Extensive groundwater extraction has been ongoing since the 1950s to meet Bologna's municipal water demand, producing pronounced declines in hydraulic head (Zuccarini et al. 2024). Figure 3 identifies the four principal municipal wellfields. Wellfields P1, P2, and P3 are situated along the Reno River, whereas P4 lies to the east of Bologna at margin of the suburban area, toward the Lamone River. Each wellfield comprises multiple production wells: P1 through P3 each are composed of 13 wells, while 6 wells are located in P4. Well depths differ considerably; the bottoms extend from 253 to 426 m below ground level. All wells draw from the confined aquifer system, i.e. pumping occurs between 62 and 157 m below ground. The effective screened lengths of the wells average 280 m at P1, 187 m at P2, 170 m at P3, and 174 m at P4.

Figure 4 summarizes the annual groundwater extraction volumes of the four municipal pumping stations over the period from 1976 to 2021, based on the most recent dataset made available from Regional Agency for Prevention, Environment and Energy of Emilia-Romagna, Italy (ARPAE). At San Vitale (P1) the abstraction fluctuates between roughly $4.0 \times 10^6\ m^3$ and $1.6 \times 10^7\ m^3$ per year. Tiro a Segno (P2) displays a similar range, varying from about $5.2 \times 10^6\ m^3$ to $2.0 \times 10^7\ m^3$. Borgo Panigale (P3) records the highest withdrawal of approximately $1.85 \times 10^7\ m^3$ in 1977 and the lowest value of $8.0 \times 10^6\ m^3$ in 1987. Fossolo (P4) consistently yields smaller volumes, ranging from about $2.1 \times 10^6\ m^3$ to $6.5 \times 10^6\ m^3$ per year. Although all stations operate within the same order of magnitude, the year-to-year variability is considerable.

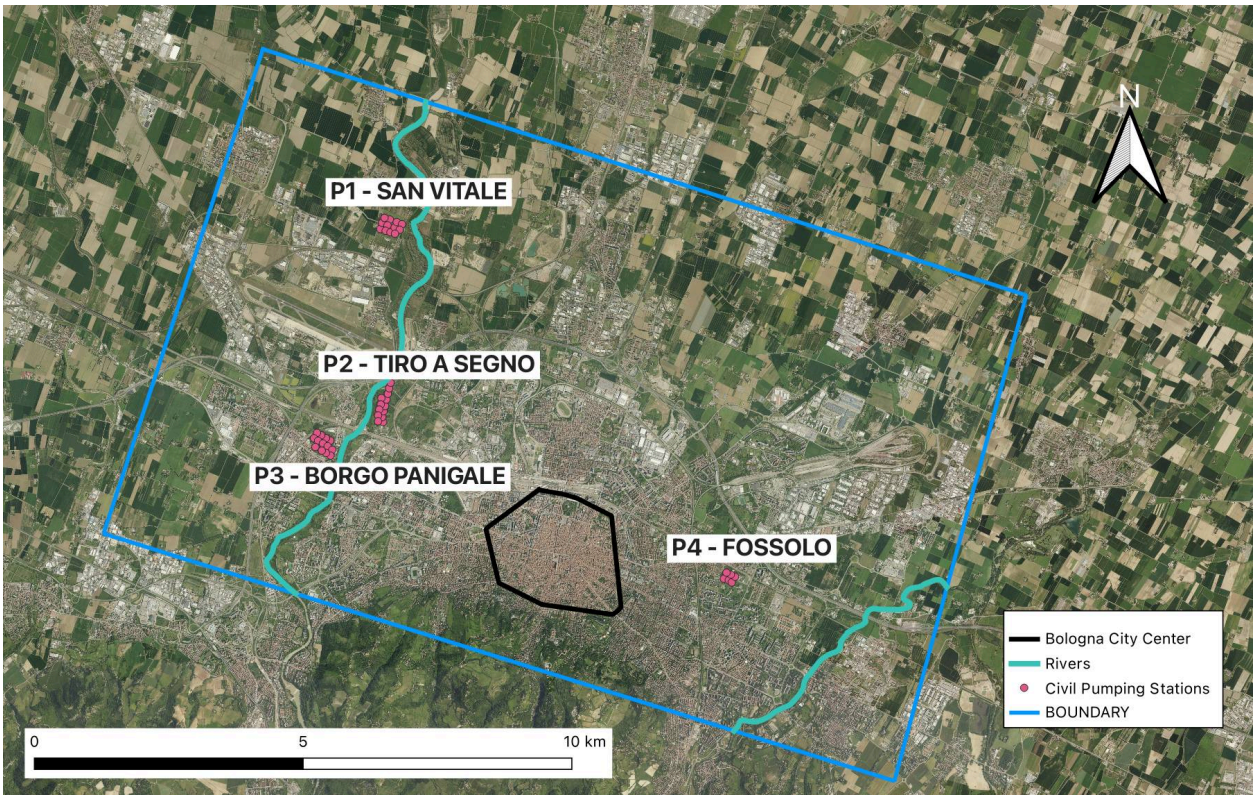

Figure 3 - The location of the municipal wellfields in Bologna

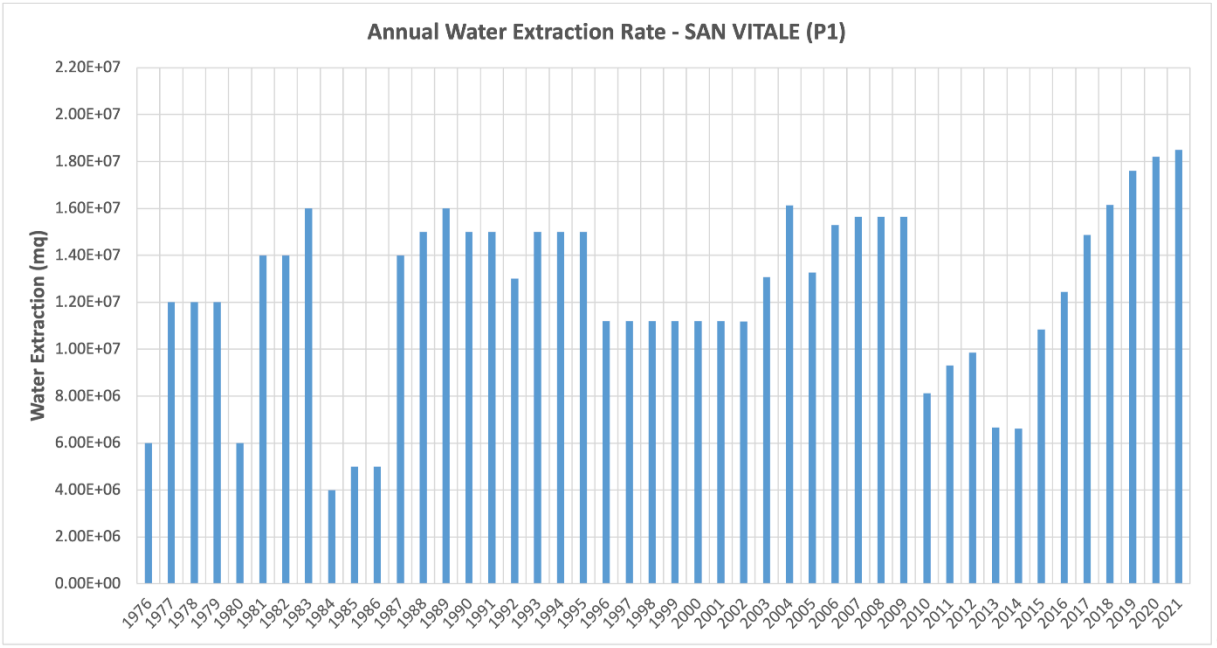
Annual Water Extraction Rate - SAN VITALE (P1)
Water Extraction (mq)
2.20E+07
2.00E+07
1.80E+07
1.60E+07
1.40E+07
1.20E+07
1.00E+07
8.00E+06
6.00E+06
4.00E+06
2.00E+06
0.00E+00
1976 1977 1978 1979 1980 1981 1982 1983 1984 1985 1986 1987 1988 1989 1990 1991 1992 1993 1994 1995 1996 1997 1998 1999 2000 2001 2002 2003 2004 2005 2006 2007 2008 2009 2010 2011 2012 2013 2014 2015 2016 2017 2018 2019 2020 2021

(a)

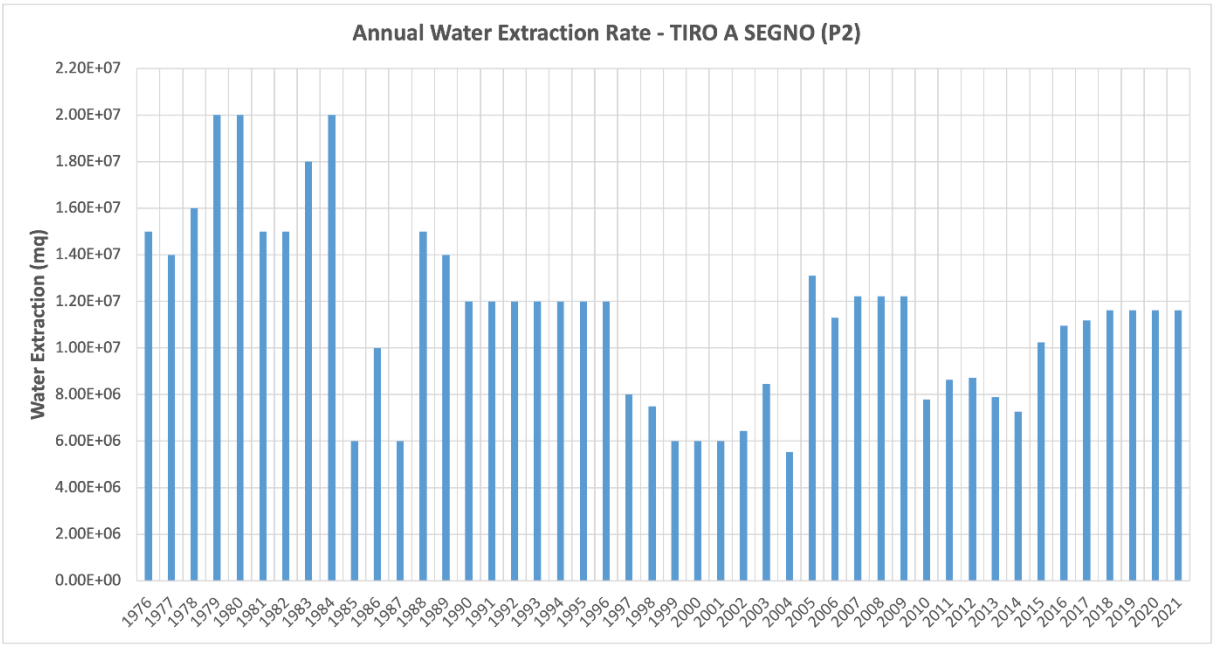
Annual Water Extraction Rate - TIRO A SEGNO (P2)
Water Extraction (mq)
2.20E+07
2.00E+07
1.80E+07
1.60E+07
1.40E+07
1.20E+07
1.00E+07
8.00E+06
6.00E+06
4.00E+06
2.00E+06
0.00E+00
1976 1977 1978 1979 1980 1981 1982 1983 1984 1985 1986 1987 1988 1989 1990 1991 1992 1993 1994 1995 1996 1997 1998 1999 2000 2001 2002 2003 2004 2005 2006 2007 2008 2009 2010 2011 2012 2013 2014 2015 2016 2017 2018 2019 2020 2021

(b)

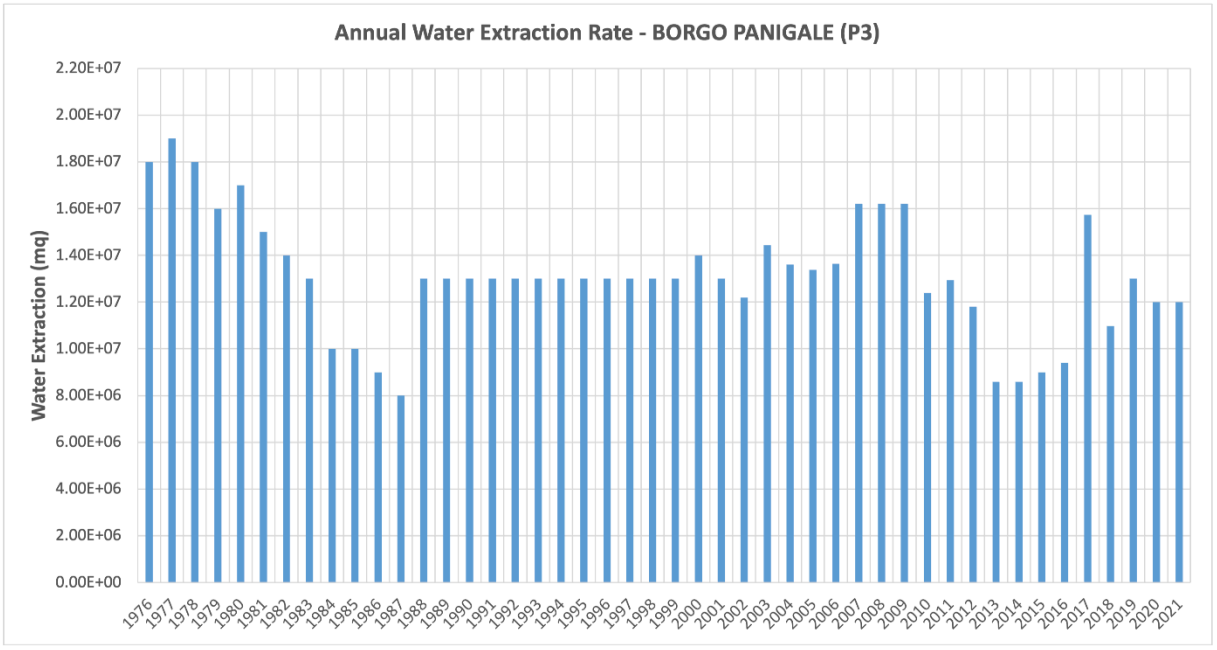

(c)

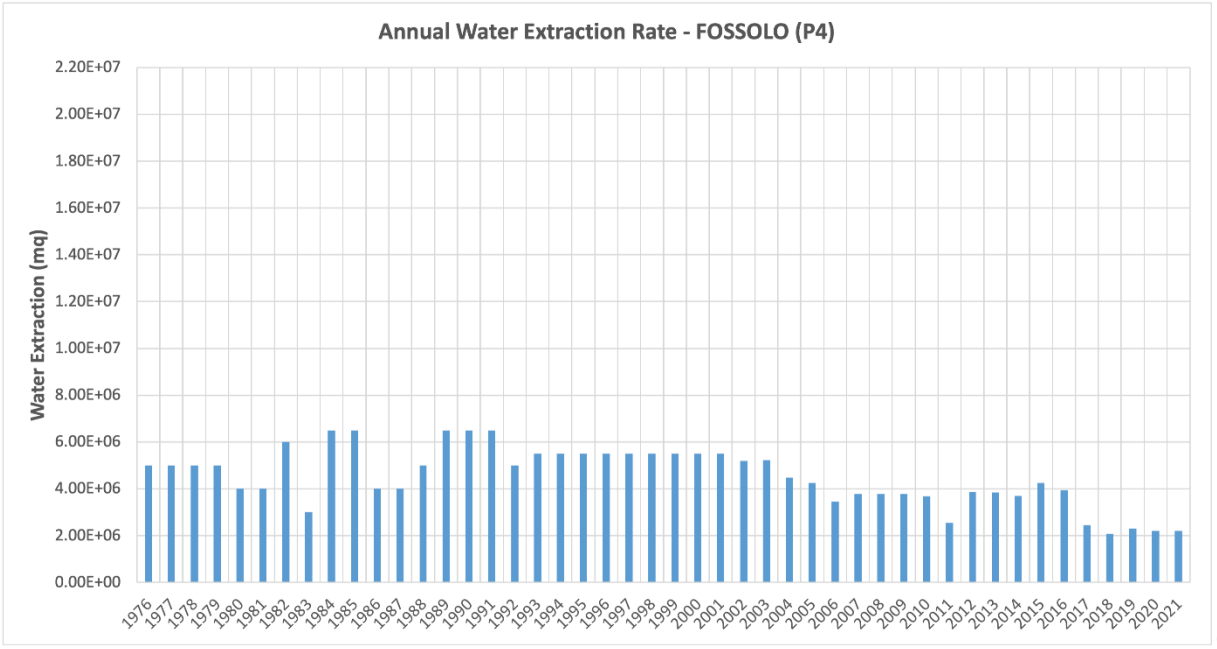

(d)

Figure 4 - Yearly groundwater volume (m3) withdrawn from the four wellfields operated around Bologna for civil purpose: (a) San Vitale – P1; (b) Tiro a Segno – P2; (c) Borgo Panigale – P3; (d) Fossolo – P4

The aquifer system has been exploited for industrial purposes. ARPAE provided a map with the location of the main industrial wells and the yearly pumping rate over the period 2002 to 2018. The values have been extended linearly to 2021; No industrial pumping was assumed before 2002. The well locations are provided in Figure 5 together with the yearly pumping rates. To be noticed that the groundwater volume extracted for industrial purposes is significantly smaller than that withdrawn from the city wellfield.

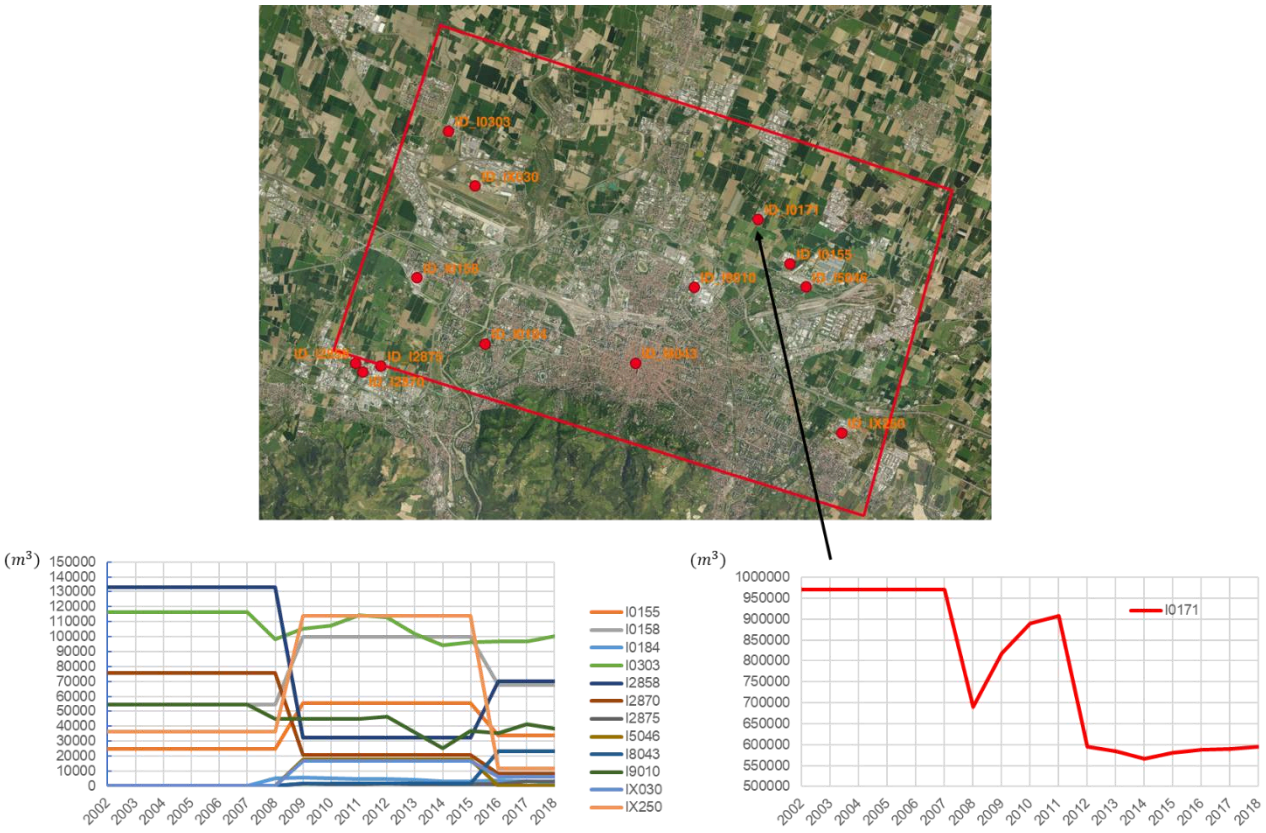

Figure 5 – Location and yearly groundwater volume (m^3) withdrawn from the industrial wells operated around Bologna. Note the different range of the y-axis of the panel relative to well IO171

2.1.4. Rainfall and aquifer recharge

Bologna, located in the south-central Po Plain, experiences a mid-latitude, temperate, humid-subtropical climate with four distinct seasons. Summers are typically hot and humid, whereas winters are cool to cold and often foggy. Mean annual precipitation is approximately 650 to 850 mm, but the distribution throughout the year is uneven. The principal wet periods occur in April to May and in October to November, with October recording the highest monthly average of about 70 mm. In contrast, January and February are the driest months, each receiving roughly 30 mm. Although summer months are generally dry, they are occasionally interrupted by short-lived, high-intensity thunderstorms.

By analyzing the data which can be downloaded in the ARPAE website (https://www.arpae.it/it/temi-ambientali/meteo/report-meteo/bollettini-mensili/bm_202304.pdf), we

know that 80 to 85% of effective groundwater recharge from precipitation mainly takes place between October and April, when soil moisture is greatest and the regional hydraulic gradient toward the plain is most pronounced owing to elevated evapotranspiration during summer.

To simplify the representation of groundwater recharge, we incorporate only annual precipitation totals in this report. The bar chart in Figure 6 displays the average annual precipitation for each year from 2001 to 2018. Although the yearly values are of similar magnitude, they still exhibit notable variability, ranging from roughly 470 mm in the driest year to more than 900 mm in the wettest year. The records have been extrapolated with a 2-degree polynomial to encompass the estimate of the data from 1976-to 2000 and after 2018 (Figure 7).

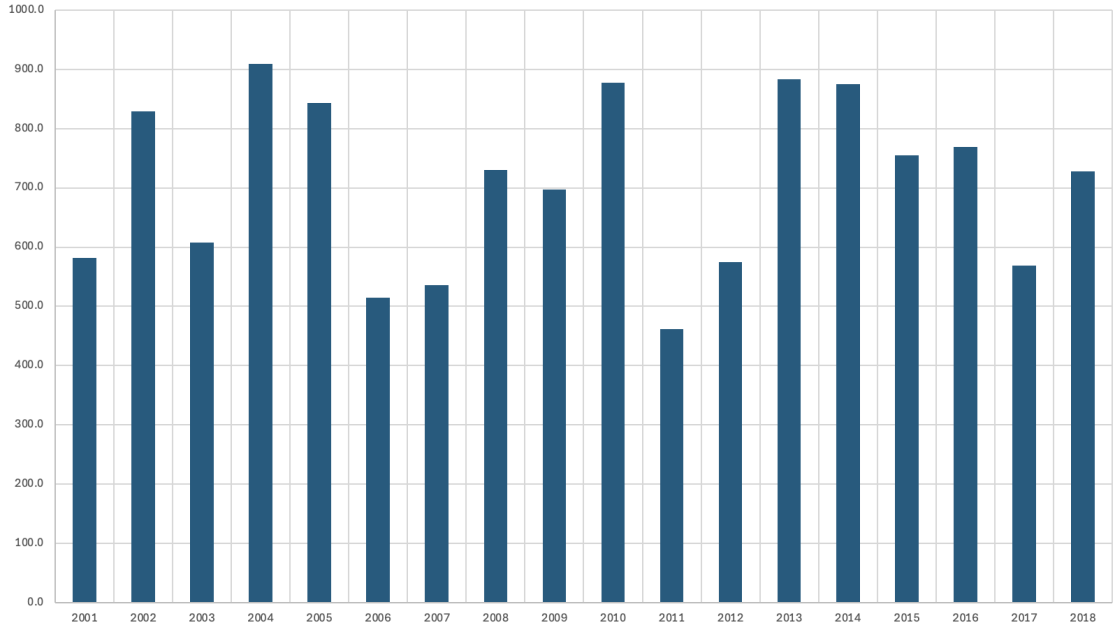

Figure 6 – Annual average precipitation (mm) on the Bologna area

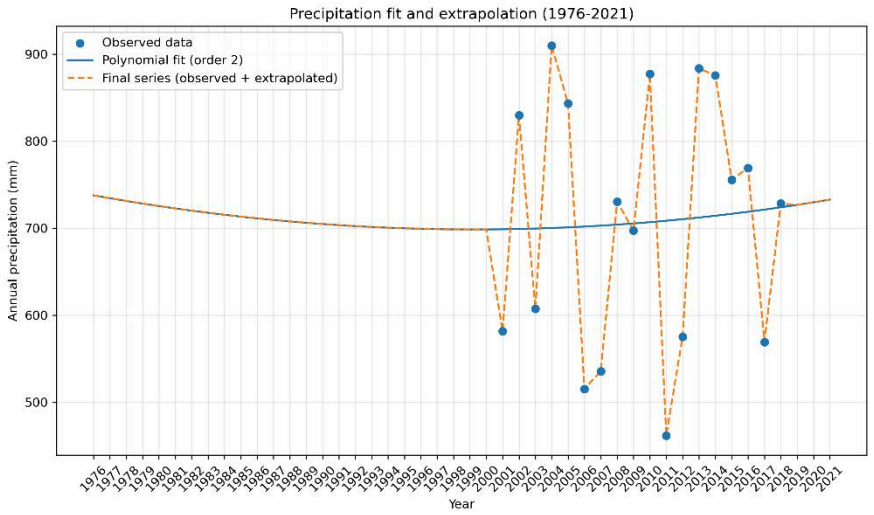

Figure 7 – Extrapolation of the annual average precipitation (mm) on the Bologna area using a 2-order polynomial

ARPAE also provided the outcome of CRITERIA, which is a post-processor providing the components of the water mass balances of a groundwater flow model developed at the regional scale. This information presents the quantity of rainfall reaching the aquifer system and is given on a square grid of 1-km size (Figure 8). This effective recharge varies between 5 and 30% of the precipitation. Consequently, an average 20% of the annual cumulative precipitation has been assumed to recharge the confined system.

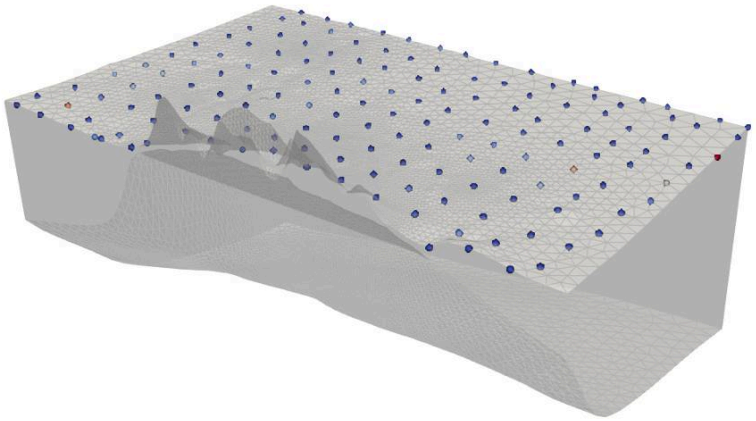

Figure 8 – Example of the distribution of the effective recharge on the CRITERIA grid as provided by ARPAER. Different colours represent different percentage of precipitation recharging the deep aquifer system

2.1.5. Available data from InSAR

Ground movement measurements in the Bologna study area are provided by Interferometric Synthetic Aperture Radar (InSAR) data. In the present study, the earliest available InSAR observations date back to 1992, whereas the most recent dataset adopted extends to 2022. The available InSAR records are derived from three different satellite sources, each corresponding to a specific observation period. More specifically, the data covering the period 1992–2000 are obtained from the European Remote Sensing Satellite (ERS), the data for the period 2006–2016 are provided by RADARSAT, and the data for the period 2018–2022 are obtained from the European Ground Motion Service (EGMS). ERS and RADARSAT were obtained from the regional subsidence monitoring project of Emilia-Romagna region (https://www.arpae.it/it/temi-ambientali/suolo/subsidenza/la-rete-regionale-di-monitoraggio-della-subsidenza). The vertical component of the displacement has been used.

Because these three datasets originate from different satellite missions and cover different temporal windows, they provide complementary information on the long-term evolution of land movements in the study area. Taken together, they allow the reconstruction of land-subsidence and ground-movement patterns over nearly three decades, thus providing an essential observational basis for evaluating the performance of the geomechanical model and for constraining the uncertainty associated with the simulated displacement response.

Figure 9 to Figure 11 show the spatial distribution of the InSAR measurement points within the study area for these three observation periods, respectively. These figures illustrate the different

spatial coverages and data availability associated with the ERS, RADARSAT, and Sentinel-1 datasets adopted in the present analysis.

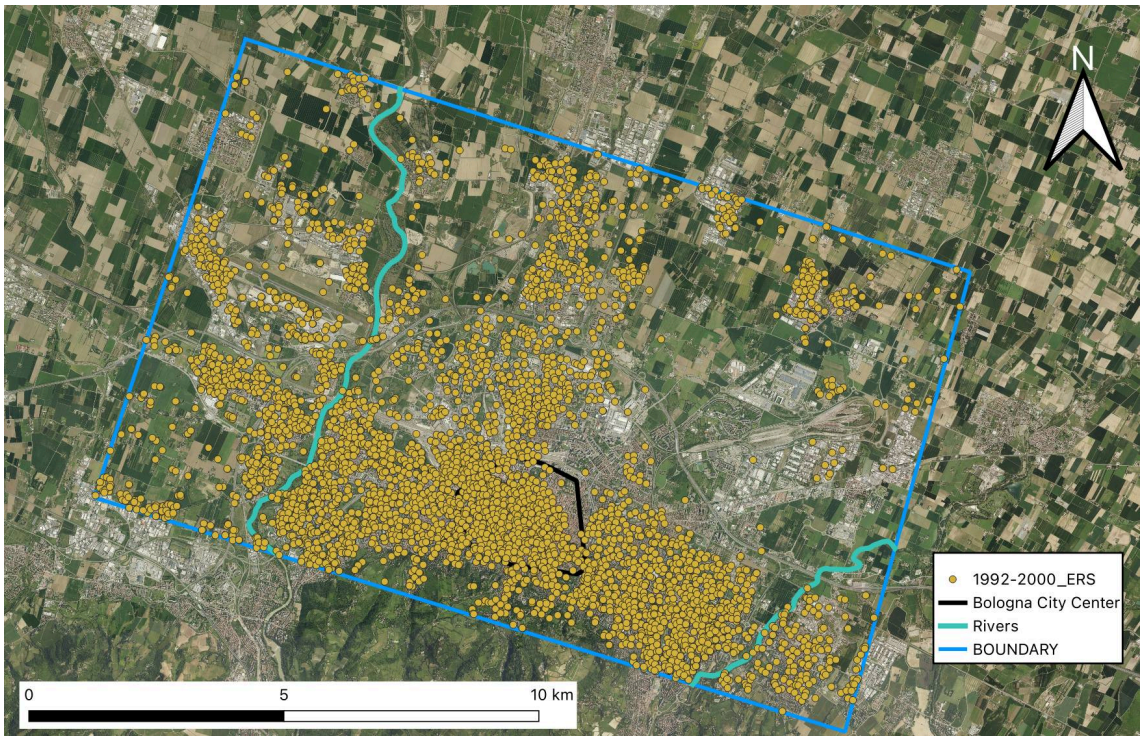

Figure 9 – InSAR data from 1992 to 2000 by ERS

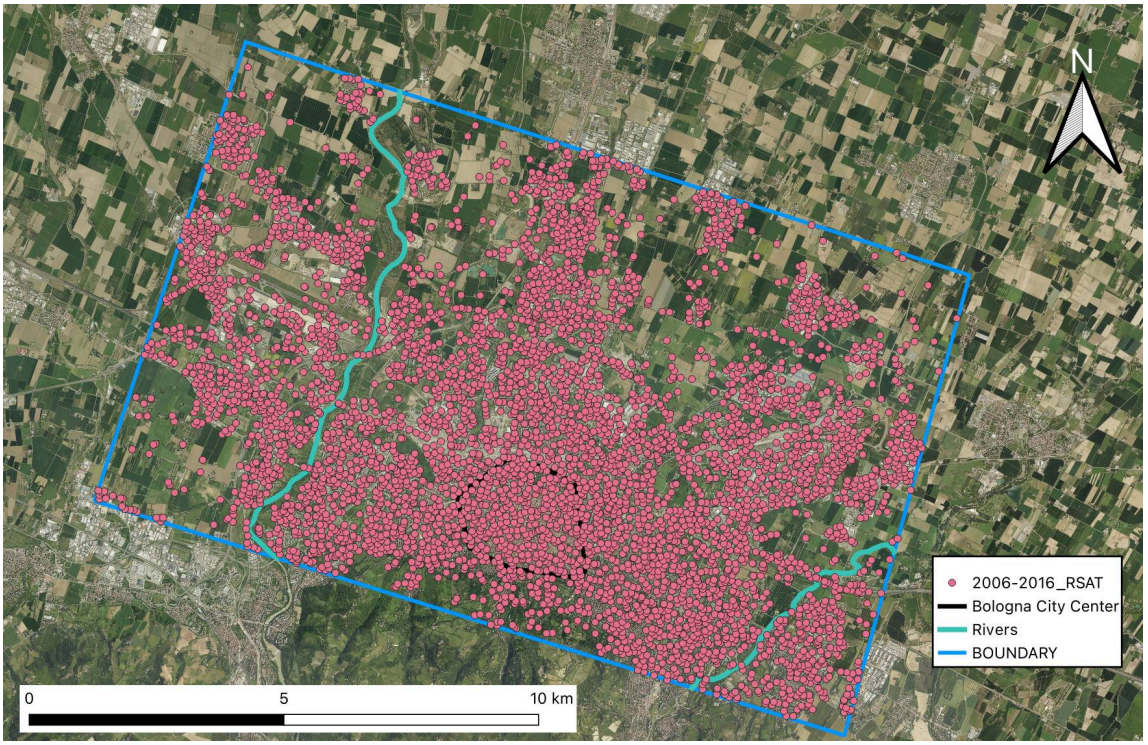

Figure 10 – InSAR data from 2006 to 2016 by RADARSAT

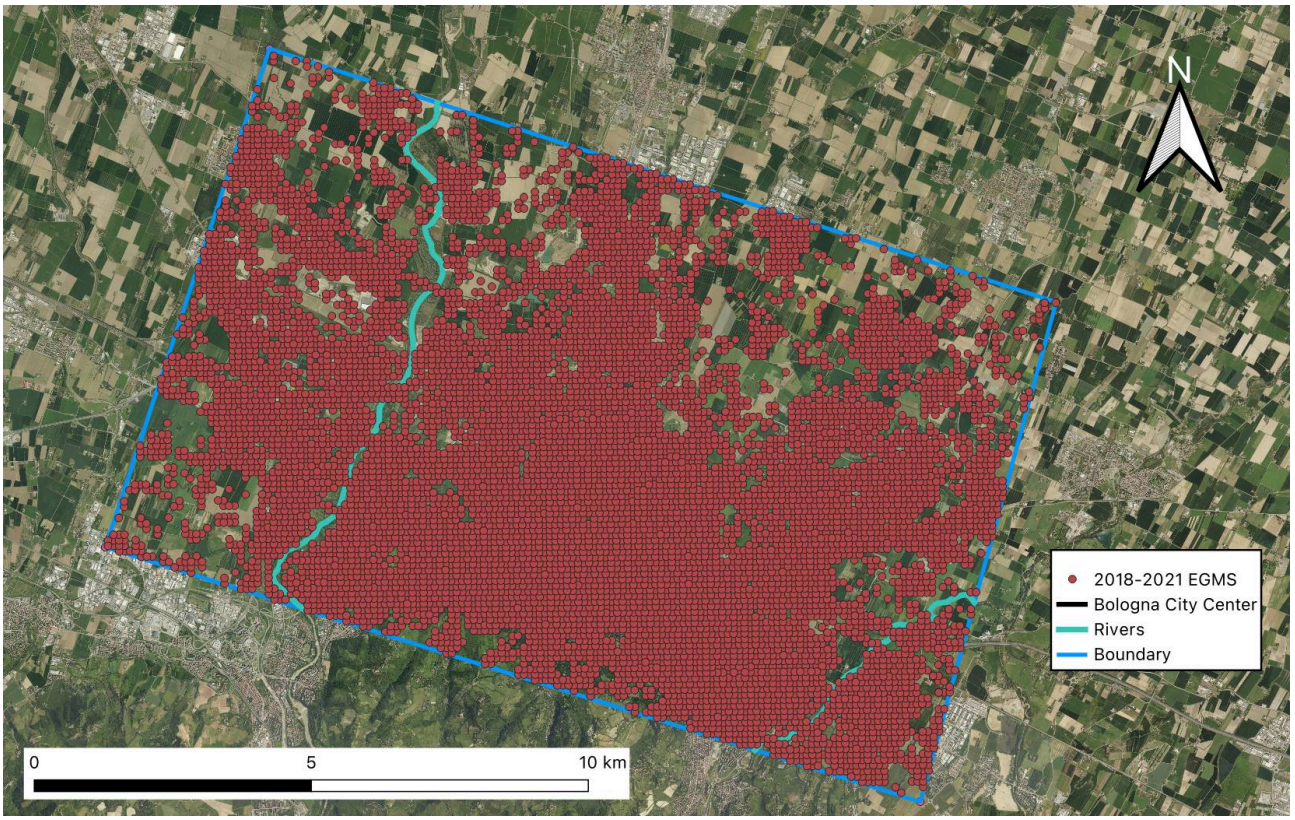

Figure 11 – InSAR data from 2018 to 2022 by EGMS

2.2. Methodologies

2.2.1. The numerical simulators

To simulate the temporal evolution and spatial distribution of the three-dimensional pore-pressure field induced by groundwater withdrawal, together with the associated displacement field, a coupled hydro-geomechanical modelling framework is adopted. In theory, the most general and rigorous formulation for this purpose is the fully coupled three-dimensional poroelasticity model (Biot 1941), in which groundwater flow and mechanical deformation are solved simultaneously.

However, in the Bologna study area, ground deformation is assumed to be primarily driven by groundwater extraction. Under this assumption, previous studies have shown that within the aquifer systems of the Po River basin, the accounting of hydraulic–mechanical coupling has no measurable influence on pore-pressure evolution and the resulting deformation at any relevant timescale (Gambolati et al. 2000). Because the fully coupled formulation requires the simultaneous solution of the mechanical equilibrium equations and the groundwater flow equation, it is associated with a significantly higher computational cost. Therefore, the present study adopts the traditional two-step approach (Gambolati and Freeze 1973), which results computationally less expensive allowing for a more refined domain discretization: in the first step, a three-dimensional saturated groundwater flow model is used to simulate the hydrodynamic behavior of the pumped multi-aquifer system. In the second step, land displacements along the vertical, south-to-north, and west-to-east are computed using a three-dimensional geomechanical model, in which the pore-pressure field obtained from the flow simulation is introduced as a known distributed source term.

The hydrodynamics is governed by the classical groundwater flow equation (Bear 2013):

$$\nabla(K\nabla h) = S_s \frac{\partial h}{\partial t} + q \qquad (1)$$

where h is the hydraulic head, t is time, q the source/sink term, K is the hydraulic conductivity tensor with principal components K_{xx}, K_{yy}, and K_{zz}, and S_s is the specific elastic storage.

On the other hand, the geomechanical equilibrium equations for a three-dimensional saturated porous medium read as:

$$\nabla\cdot(\sigma - bPI) = f \qquad (2)$$

where σ is the effective stress, b is the Biot coefficient, P is the pore fluid pressure, I is the identity tensor, and f is the set of external forces. In the present analysis, we assume the porous medium to be isotropic elastic with incompressible solid grain (i.e., b=1). Equation (2) can be written in terms of displacements as follows (Verruijt, 1969):

$$G\nabla^2 u_i + (\lambda + G)\frac{\partial \epsilon}{\partial i} = \frac{\partial p}{\partial i} + f_i \qquad i = x, y, z \qquad (3)$$

where G is the shear modulus, λ is the Lamé first parameter, ϵ is the volumetric strain, p is the hydraulic head, and u_i is the displacement component along the i-th coordinate direction of a standard Cartesian reference.

Equation (3) can be further simplified alone with the Lamé first parameter:

$$\lambda = \frac{E\nu}{(1+\nu)(1-2\nu)} \tag{4a}$$

$$\frac{E}{2(1+\nu)}\left(\frac{1}{1-2\nu}\frac{\partial \epsilon}{\partial i} + \nabla^2 u_i\right) = \frac{\partial p}{\partial i} + f_i \qquad i = x, y, z \tag{4b}$$

where E and ν are the Young's modulus and Poisson ratio, respectively. Equations (1) and (4b) are coupled since:

$$P = \gamma_w \Delta H \tag{5}$$

$$S_S = \gamma_w (c_m + \phi\beta) \tag{6}$$

$$c_m = \frac{(1+\nu)(1-2\nu)}{E(1-\nu)} \tag{7}$$

where γ_w and β are the water specific weight and volumetric compressibility, respectively, ϕ is the porosity, and c_m is the oedometric compressibility of the porous medium. It should be emphasized that, in the present model, the nonlinear hysteretic mechanical behavior distinguishing virgin loading from unloading conditions, as induced by hydraulic head decline and recovery, is represented through updating the elastic constants in accordance with the c_m constitutive model.

2.2.2. Ensemble Smoother with Multiple Data Assimilation

One of the main objectives of the present study is to reduce the uncertainty in the model associated with poorly constrained parameter values, such as hydraulic conductivity and compressibility. To this end, the methodology adopted in the current analysis is the so-called Ensemble Smoother with Multiple Data Assimilation (ES-MDA) (Emerick and Reynolds 2013). The ES-MDA is an ensemble-based updating method designed for history matching in nonlinear systems. In contrast to the standard ensemble smoother, which assimilate the full observation dataset only once, ES-MDA assimilates the same dataset repeatedly over a prescribed number of assimilation steps. The key mechanism is to inflate the measurement-error covariance at each step, so that each update is intentionally smaller and more stable than a single, potentially over-aggressive correction. This "multiple, damped" updating strategy improves robustness and typically yields better data matches in nonlinear applications while retaining the practical smoother workflow.

Within the traditional two-step framework, in which the saturated groundwater flow model is coupled to the geomechanical model through specific storage, the first step, namely the solution of the transient groundwater flow problem, is typically formulated as a parameter-estimation problem. In this stage, the dominant uncertain parameters are the hydraulic conductivities assigned to the different lithofacies. Because the mapping from hydraulic conductivity K to the temporal evolution

of the hydraulic head is generally nonlinear, the use of ES-MDA is particularly appropriate. Indeed, ES-MDA is motivated by the limitation of the standard Ensemble Smoother, whose update is equivalent to a single full Gauss–Newton step and may therefore be excessively aggressive in nonlinear settings. By contrast, ES-MDA distributes the correction over several smaller assimilation steps using ensemble-based sensitivity estimates, thereby improving stability and reducing the risk of overcorrection.

In the second step of the framework, the geomechanical model is driven by the pore-pressure changes computed from the flow model, while the main uncertain parameters are the compressibility values controlling compaction and surface displacement. In this context, ES-MDA is explicitly formulated as a parameter-estimation approach rather than as a sequential state-filtering method, such as the EnKF, which is advantageous for preserving consistency between parameters and model states. This aspect is particularly important in a two-step setting, where the state variable, namely the pressure-change history, is generated by the flow model and must remain physically consistent with the updated mechanical parameters used to predict deformation. Moreover, the operator relating pressure changes and compressibility to subsidence is nonlinear over the relevant stress range. Under these conditions, ES-MDA is supported theoretically by its equivalence to the linear-Gaussian solution under appropriate assumptions and, in practice, provides a robust and stable framework for assimilating deformation observations, such as InSAR measurements, to reduce uncertainty in compressibility while limiting overcorrection.

Let $m_j^{(i)}$ be the parameter vector of ensemble member j at assimilation step i, and let $d_j^{(i)} = g(m_j^{(i)})$ be the corresponding model-predicted data obtained by running the forward model. The ES-MDA update at step i is given by the ensemble-smoother formula with inflated data-error covariance:

$$m_j^{(i+1)} = m_j^{(i)} + C_{MD}^{(i)}\left(C_{DD}^{(i)} + \alpha_i C_D\right)^{-1}\left(d_{uc,j}^{(i)} - d_j^{(i)}\right) \qquad j = 1, \ldots, N_e \tag{8}$$

where $C_{MD}^{(i)}$ is the sample cross-covariance between parameters and predicted data, and $C_{DD}^{(i)}$ is the sample covariance of predicted data, both computed from the ensemble at step i.

At each assimilation step i, ES-MDA uses perturbed observations consistent with the inflated error covariance:

$$d_{uc,j}^{(i)} = d_{obs} + \sqrt{\alpha_i} C_D^{1/2} z_{d,j} \qquad z_{d,j} \sim N(0, I) \tag{9}$$

For consistency with the linear-Gaussian case, the inflation coefficients $\{\alpha_i\}_{i=1}^{N_\alpha}$ are selected such that:

$$\sum_{i=1}^{N_\alpha} \frac{1}{\alpha_i} = 1 \tag{10}$$

Therefore, the ES-MDA algorithm follows:

Algorithm 1 Ensemble Smoother with Multiple Data Assimilation

1: Set the number of data assimilations, $N_\alpha = 100$, and the coefficients $\alpha_i = 5$ for $i = 1, \ldots, N_\alpha$;
2: **for** $i = 1, \ldots, N_\alpha$ **do**
3: Run the ensemble from time zero;
4: For each ensemble member, perturb the observation vector using $d_{uc} = d_{obs} + \sqrt{\alpha_i} C_D^{1/2} z_d$
5: Update the ensemble using Eq (8) with C_D replaced by $\alpha_i C_D$
6: **end for**

3. SET-UP OF THE MODELLING FRAMEWORK

3.1. Groundwater flow model (SAT3D)

3.1.1. Steady state

The evolution of the piezometric head in the Bologna aquifer system is simulated using SAT3D, a three-dimensional saturated flow simulator developed by the Department of Civil, Architectural and Environmental Engineering of the University of Padova. In the current application, the simulator was used in two phases: a steady-state analysis, used to provide the initial hydraulic condition for the starting year 1976, and lately a transient analysis, used to simulate the hydrodynamic evolution during the period of interest encompassing the period 1976 to 2021.

According to Eq. (1), the temporal term vanishes under steady-state conditions since $\partial h/\partial t = 0$. Therefore, only the Dirichlet boundary condition is strictly required to solve the steady-state problem, whereas the initial condition and the Neumann condition can be set to zero. In the present flow model, the Dirichlet boundary condition represents the hydraulic head distribution along the boundary of the numerical domain, which coincides with the study area boundary shown in Figure 1. However, since the available hydraulic data for 1976 consist of measurements from only 29 piezometric monitoring wells, spatial interpolation was first performed to estimate the hydraulic head distribution across the entire study area for that year. This enabled the assignment of hydraulic head values along the model boundary. The interpolated values were then prescribed at the boundary nodes of the numerical model, thus completing the specification of the Dirichlet. The pumping rates in 1976 at the four municipal wellfields were also introduced in the steady-state simulation.

Figure 12 shows the hydraulic head map for 1976 obtained by interpolating measurements from the 29 piezometric monitoring wells, while Figure 13 presents the initial hydraulic condition for 1976 simulated by SAT3D. The match is quite satisfactory, with some gentle and local discrepancies in the inner part of the domain.

The hydraulic conductivity values assigned in the steady-state model correspond to four lithological materials, namely gravel, sand, silty clay, and clay. These values were adopted from empirical ranges, as follows:

(i) Gravel: $K_X = K_Y = 220\ m/day$; $K_Z = 22\ m/day$

(ii) Sand: $K_X = K_Y = 110\ m/day$; $K_Z = 11\ m/day$

(iii) Silty clay: $K_X = K_Y = 10^{-5}\ m/day$; $K_Z = 10^{-6}\ m/day$

(iv) Clay: $K_X = K_Y = 10^{-6}\ m/day$; $K_Z = 10^{-7}\ m/day$

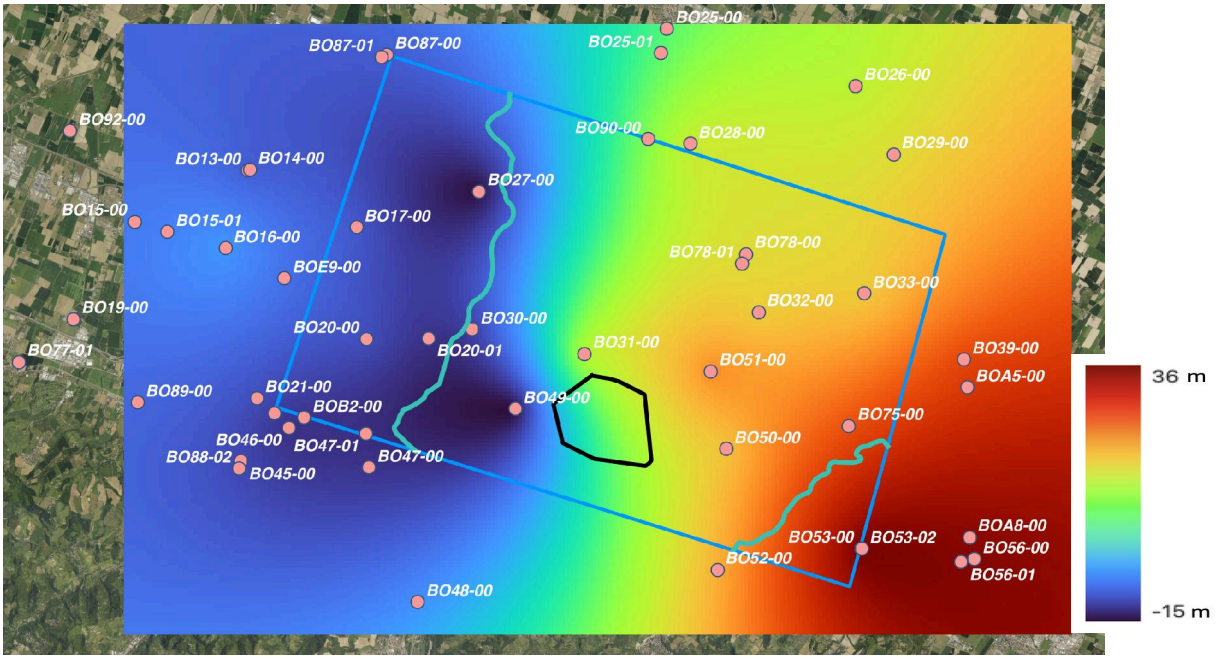

Figure 12 – Hydraulic head in 1976 interpolated by the records from 29 piezometric monitoring wells

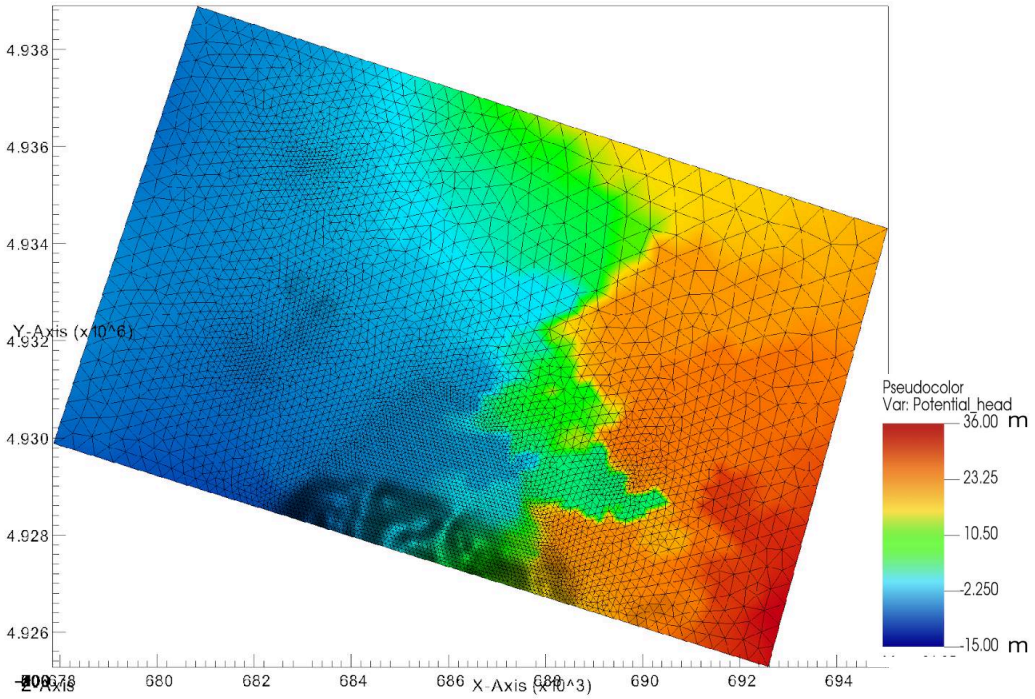

Figure 13 – Hydraulic heads in 1976 as calculated by the steady state flow model

With piezometric records referring to a natural "undisturbed" condition, this procedure would be sufficient to establish the steady-state hydraulic field to be used as the initial condition for the transient model. However, the intensive groundwater extraction had already been ongoing for several years prior to 1976; therefore, it is reasonable to assume that the hydraulic heads provided by the piezometers in that year were not in equilibrium.

If the hydraulic heads in 1976 were not in equilibrium, the monitoring network records would only represent conditions within the gravel and sand lithofacies due to their relatively high hydraulic conductivity. The available measurements can reasonably represent the imposed boundary conditions for these lithologies. In contrast, pore pressures within the silty clay and clay lithofacies are expected to be substantially higher (i.e., smaller piezometric drawdown) than the simulated values because the hydraulic conductivity of these two lithofacies is low. Consequently, if the steady-state model outputs shown in Figure 13 were used directly under this configuration, pore pressures decline within the clay and silty clay units would be significantly overestimated.

A specific treatment was therefore required to account for this consideration. The hydraulic heads within the clay and silty clay layers were manually adjusted on the basis of the steady-state simulation results. More specifically, based on longer piezometric records (Teatini et al., 1995) or similar analyses (Teatini et al., 2006) available for other portions of the Po Plain aquifer system, it was assumed that, prior to the onset of groundwater extraction, the pore pressure within the aquifer system was equal to the DEM value at the corresponding location. The difference between these reference values and the hydraulic heads computed by the steady-state numerical model at the same points is then calculated and defined as Δ. To compensate for the overestimation of the pressure decline produced by the steady-state solution, a certain portion f of Δ was returned to the clay and silty-clay elements layers. The best value of this factor was calibrated by a trial-and-error procedure and was quantified in 80% for the clay lithofacies and 70% of Δ for the silty clay lithofacies. This assumption proved to be both reasonable and essential for reproducing the delayed subsidence response observed in the numerical simulations.

A couple of figures are added before to explain more clearly the outcome of this adjustment to the steady state solution. Figure 14 shows a representative cross section of the pore-pressure field produced by the steady-state flow model, extending across the pumping stations and the margin of the city center. Figure 15 presents the same cross section after applying the adjustment described above. It is evident that, after this correction, the pore-pressure distribution becomes more realistic, with pressures more clearly differentiated among layers characterized by different hydraulic conductivities and with sharper boundaries between adjacent lithological units.

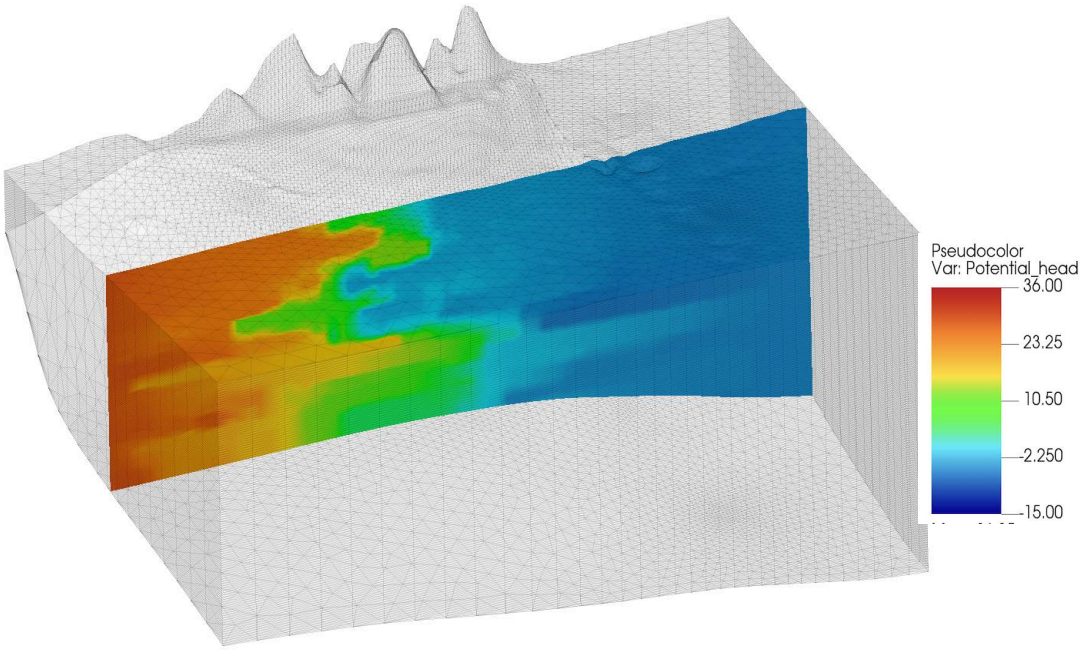

Figure 14 – A representative cross section showing the pore-pressure field produced by the steady state flow model

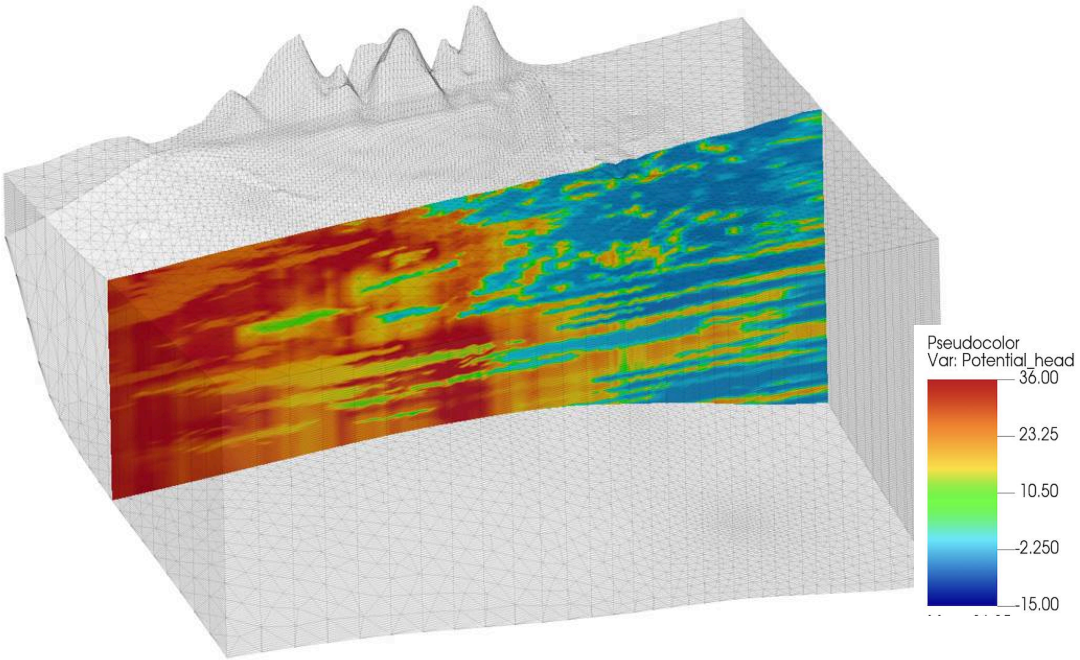

Figure 15 – The same representative cross section of Figure 14 with the adjusted pore-pressure field in the less permeable lithofacies

3.1.2. Transient state

Transient groundwater flow simulations were run using as initial conditions the outcome of the steady state adjusted as described above. Dirichlet boundary conditions and Neumann boundary conditions were assigned in order to reproduce the past hydrodynamic evolution over the period 1976 to 2021.

The Dirichlet boundary conditions in the transient model were updated on a yearly basis. The procedure adopted to assign these boundary values was the same as that used for the steady-state model. Specifically, all available piezometric data for a given year were used to generate, by kriging interpolation, a map of the hydraulic head distribution over the study area. The interpolated values along the boundary of the numerical domain are then assigned as Dirichlet boundary conditions in the transient model. This procedure is repeated for each simulated year in the historical period.

The Neumann boundary conditions are defined in terms of the discharge and recharge rates during the simulated period. Under the assumption that pore-pressure changes in the study area are mainly induced by anthropogenic activities, groundwater extractions for civil and industrial use were prescribed as the discharge component of the Neumann boundary condition, whereas effective precipitation over the study area was prescribed as the recharge component. A proper tool has been implemented to assign the withdrawn rates to permeable facies (gravel and silt) only along each vertical column corresponding to the wells. Also, the effective recharge was assigned to the surface elements corresponding to permeable facies, with a proper redistribution procedure implemented to maintain the cumulative infiltration volume.

3.2. Geomechanical model (SUB3D)

The geomechanical simulator used in the present report to reproduce land subsidence and horizontal displacements is SUB3D, which was also developed by the Department of Civil, Architectural and Environmental Engineering of the University of Padova and largely used in previous applications worldwide (e.g., Ochoa-Gonzalez et al., 2018; Zhu et al., 2020). Like SAT3D, SUB3D requires the specification of Dirichlet boundary conditions, whereas the Neumann conditions are represented by body forces. In SUB3D, the Dirichlet boundary conditions are defined in terms of nodal displacements. Accordingly, the displacement of all nodes at the bottom of the model is constrained to zero, while the lateral and surface nodes are left free to move. Nauman conditions are represented by the pressure change over space and time as computed by SAT3D.

Because the hydraulic head evolution in the study area has undergone both discharge and recharge phases, and because ground-surface displacement is assumed to be primarily induced by these pore-pressure changes, the system is expected to have experienced both loading and unloading conditions. Consequently, once the effective stress exceeds the preconsolidation stress, the resulting subsidence becomes irreversible, and the compressibility governing this behavior must differ from that associated with the unloading, or elastic phase. To account for this mechanism, SUB3D is formulated as an elastoplastic model and is able to automatically assign different compressibility values according to the prevailing loading or unloading condition. Previous studies have shown that the shallower the soil layer, the greater the ratio c_r between loading and unloading compressibilities (Teatini et al. 2006). Therefore, in the present study, a value of was calibrated on the InSAR measurements by a trial-and-error procedure yielding a best value equal to $c_r = 50$, which is in the

range of variability for an aquifer system spanning a few hundred meters depth (Teatini et al., 2011).

4. RESULTS

4.1. Piezometric evolution

4.1.1. Initial tests using SAT3D and prior ensembles

In this section, the analysis focuses primarily on the results produced by the transient groundwater flow model, as these outputs correspond to the model-predicted data in the ES-MDA data assimilation framework. Within this framework, the transiently simulated hydraulic heads constitute one of the principal components of the assimilation procedure, along with the observed data and the uncertain material parameters to be updated. In contrast, the results of the steady-state flow model do not enter the assimilation procedure explicitly; their role is limited to providing the initial hydraulic condition for the subsequent transient simulations.

To represent parametric uncertainty in the groundwater flow model, 100 different sets of hydraulic conductivity values were generated automatically based on empirical ranges for the four lithofacies considered in the study: gravel, sand, silty clay, and clay. Since production wells predominantly tap permeable units and groundwater is primarily conveyed through the gravel and sand units—where piezometric observations are collected—while conditions in the silty clay and clay units cannot be observed directly, the present analysis primarily aims to reduce the uncertainty associated with the hydraulic conductivity of gravel and sand. These two lithofacies therefore represent the principal target parameters in the data assimilation process.

The 100 sets of hydraulic conductivity values differ in the values assigned to gravel and sand, being both characterized by a uniform distribution. For the gravel lithofacies, the hydraulic conductivity in the vertical direction, K_z, is allowed to vary from 1 m/day to 100 m/day. The horizontal hydraulic conductivities, K_x and K_y, are assumed to be ten times greater than K_z, thereby reflecting anisotropic hydraulic behavior. For the sand lithofacies, the vertical hydraulic conductivity ranges from 10^{-2} m/day to 1 m/day, while the horizontal conductivities are again taken as ten times the corresponding vertical values. In contrast, the hydraulic conductivity values assigned to the silty clay and clay lithofacies are kept fixed throughout the ensemble generation. Specifically, the vertical hydraulic conductivity is set equal to 10^{-6} m/day for silty clay and 10^{-7} m/day for clay, with the horizontal conductivities in both cases assumed to be ten times larger than the corresponding vertical values.

The 100 realizations of hydraulic conductivity for gravel and sand are generated using the Latin Hypercube Sampling (LHS) method. This sampling strategy is adopted to ensure efficient and statistically representative exploration of the prescribed parameter ranges. Specifically, LHS guarantees that the sampled values are distributed approximately uniformly across their respective domains while ensuring that each subinterval of the parameter space is sampled in a balanced manner. In this way, the ensemble captures the prior uncertainty of the hydraulic conductivity

parameters before the assimilation of observational data. These 100 parameter sets are therefore referred to as the prior ensemble.

Figure 16 shows the cumulative distribution functions (CDFs) of the two lithofacies considered in the present study, namely gravel and sand. The blue curve corresponds to gravel, whereas the orange dashed curve corresponds to sand. Both CDFs exhibit an approximately linear increase, indicating that the sampled values are distributed nearly uniformly in logarithmic space over their prescribed domains. This pattern is consistent with the Latin Hypercube Sampling (LHS) strategy adopted in the present analysis, which is intended to ensure an even exploration of the parameter ranges and a balanced representation of prior uncertainty for both lithofacies.

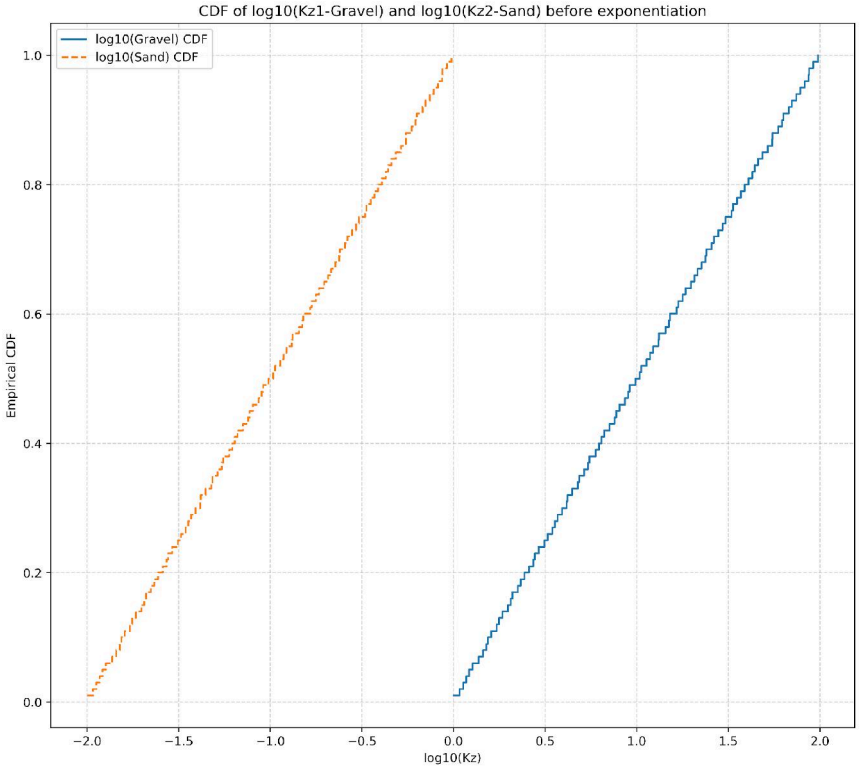

Figure 16 - Empirical cumulative distribution functions of the sampled (K_z) values for gravel and sand

The simulated hydraulic head obtained from this prior ensemble over the period from 1976 to 2021, during which the model is constrained by the available boundary conditions, pumping data, recharge conditions, and observational information are presented in the following Figure 17. The figure shows the temporal evolution of hydraulic heads at the locations of the four municipal pumping stations, P1 to P4. In panels, the grey curves represent the 100 model simulations generated from the prior ensemble, the orange curve represents the ensemble mean, and the blue dots correspond to the observation data. The following considerations can be drawn:

- At P1, the simulated ensemble captures the overall temporal pattern, but the observations remain systematically lower than the ensemble mean for most of the period, indicating that the prior simulations tend to overestimate the hydraulic head at this site.

- At P2, the agreement is generally better, as the ensemble mean follows the observed behavior more closely, especially during the recovery phase after 2010, although minor discrepancies remain in the earlier decades.
- At P3, the model reproduces the broad evolution of hydraulic heads, including the declining stage, the relatively stable intermediate period, and the subsequent recovery, while the observations are again gently lower than the ensemble mean, particularly during the later years.
- At P4, the mismatch is more pronounced than at the other locations, as the simulated heads are consistently higher than the observations throughout most of the record, even though the model still captures the major long-term trend. The significant pressure recovery after 2017 is significantly underestimated.

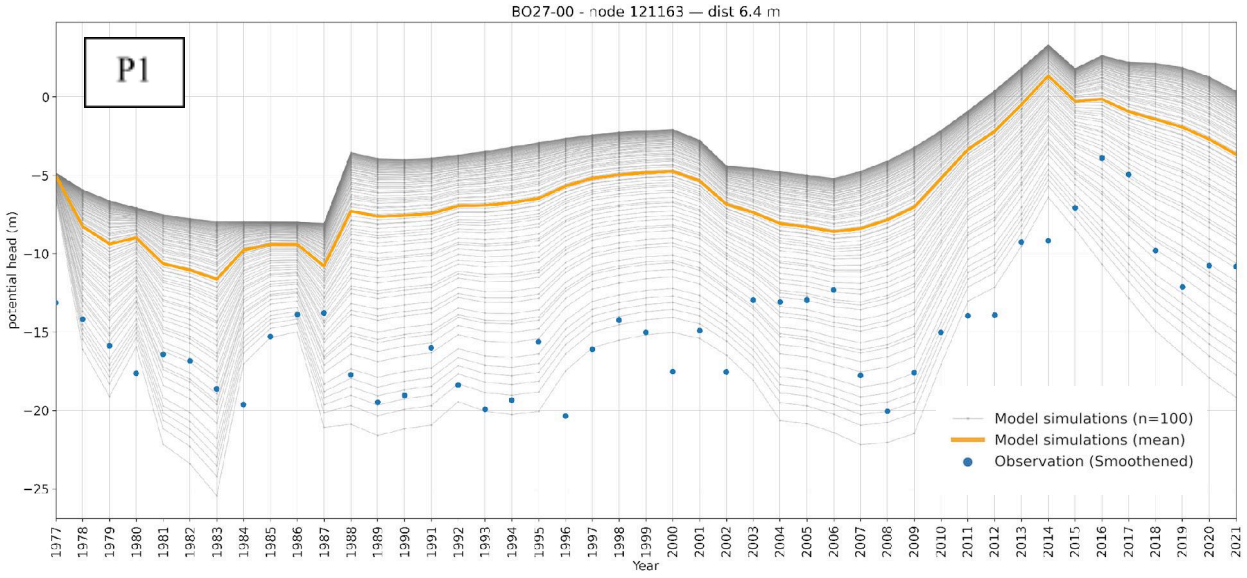

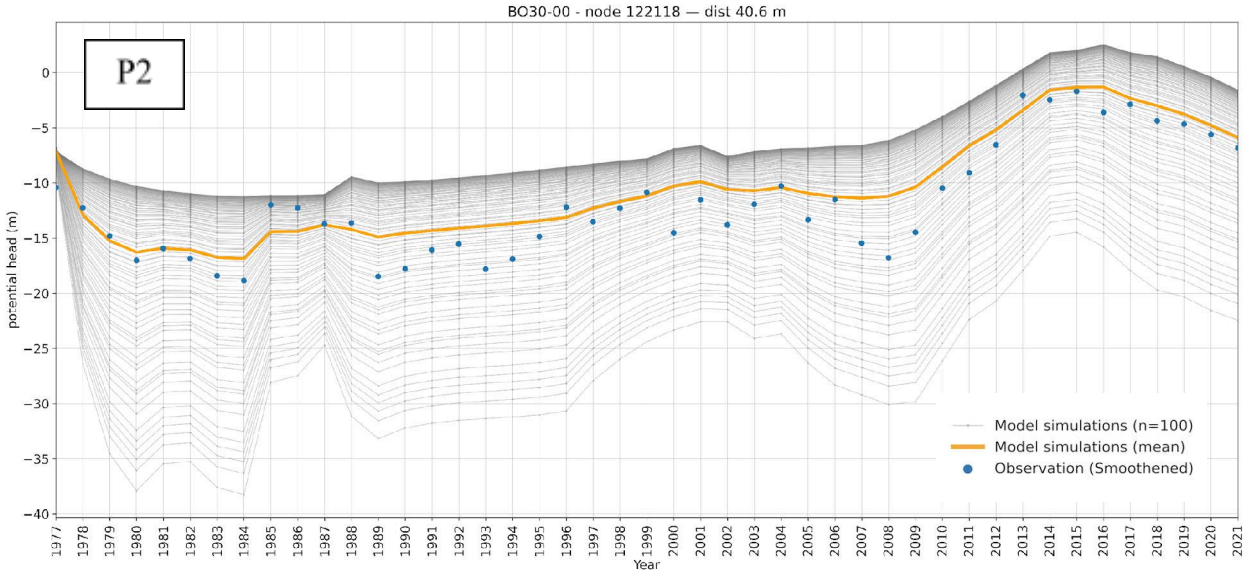

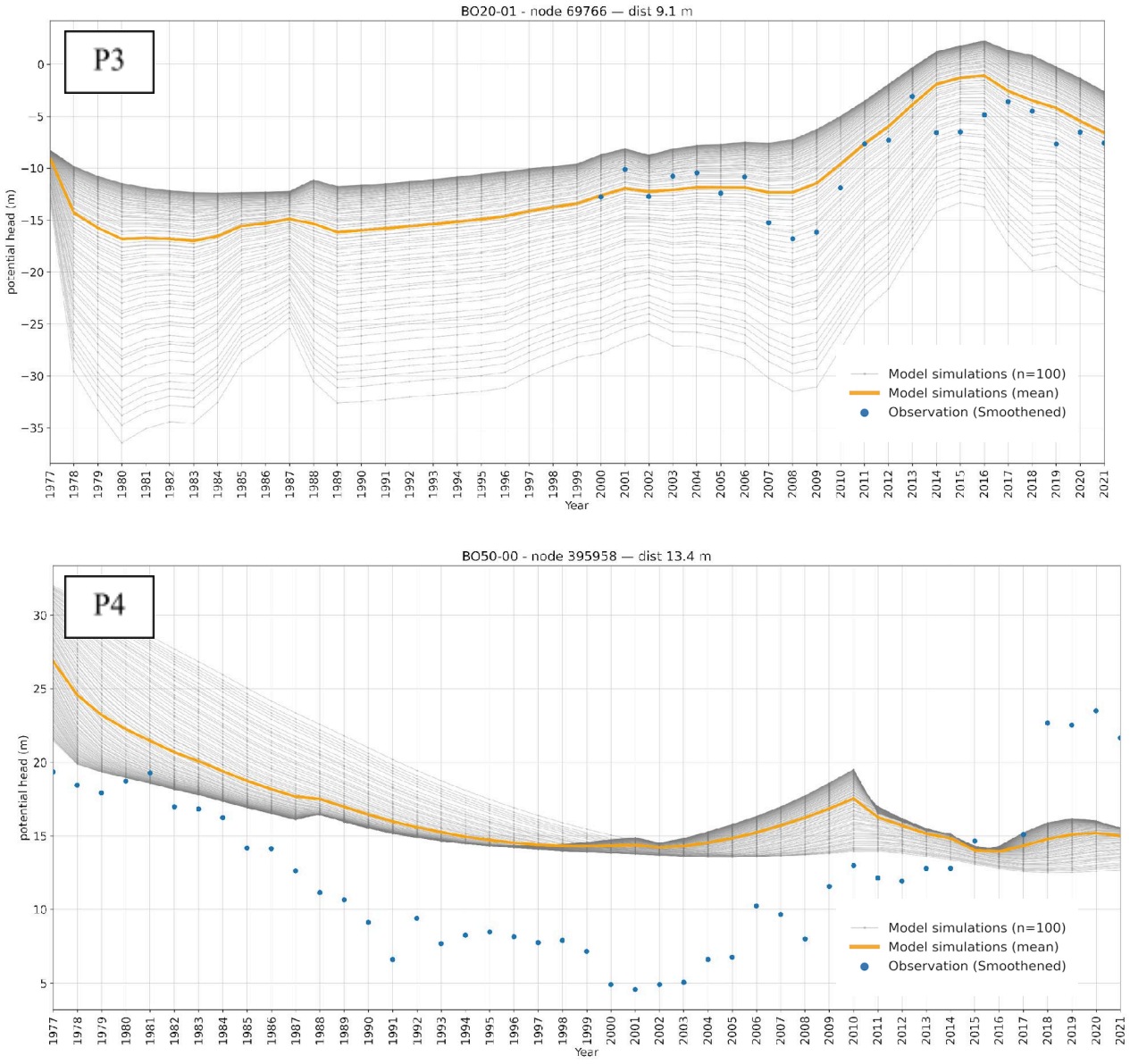

Figure 17- Temporal evolution of hydraulic head at the four representative municipal pumping stations P1–P4 during the period 1977–2021. The observations are reported together with the prior ensemble obtained by SAT3D and the mean

The direct assimilation of the simulated hydraulic heads against the observed heads would lead to substantial performance degradation, as the mismatch would be strongly influenced by errors inherited from the initial hydraulic condition rather than by the actual temporal evolution of the system. In other words, part of the discrepancy between model predictions and observations would not reflect an incorrect dynamic response of the transient flow model, but rather the uncertainty associated with the initial head distribution assigned at the beginning of the simulation. If these absolute hydraulic head values were assimilated directly, the ES-MDA procedure could incorrectly attribute such discrepancies to the hydraulic conductivity parameters, thereby producing biased updates and reducing the reliability of the calibrated model.

To offset this effect, the assimilation is performed on hydraulic head variations rather than on absolute hydraulic head values. Indeed, the geomechanical response of an aquifer system depends on pressure variations and not on absolute pressure values. Therefore, for each observation point, the hydraulic head at each simulated year is expressed as a relative difference with respect to the hydraulic head corresponding to the first year for which an observation is available at that location. The same transformation is applied consistently to both simulated and observed data. In this way, the comparison between model predictions and measurements is based on the temporal change in hydraulic head rather than on its absolute magnitude. This procedure largely removes the influence of possible inaccuracies in the initial hydraulic condition and allows the assimilation process to focus on the model's ability to reproduce the observed drawdown and recovery trends over time. Consequently, the updated parameters are constrained more effectively by the dynamic behaviour of the aquifer system, which is the quantity of primary interest in the present study

Figure 18 shows the relative differences in hydraulic head, computed with respect to the first available observation year at each monitoring location. Both the simulated and observed series start from a common baseline equal to zero, so that the comparison focuses exclusively on the temporal evolution of drawdown and recovery rather than on the absolute hydraulic-head magnitude. Overall, the figures indicate that the prior ensemble is generally able to reproduce the first-order dynamic behavior of the system, including phases of decline, stabilization, and recovery.

At P1 and P2, the simulations capture the broad long-term pattern, with an initial decline followed by a gradual recovery and a marked increase after approximately 2010. At P3, where observations are available only from 2000 onward, both the simulated and observed series show an overall rising trend after the late 2000s. At P4, the relative-difference representation highlights a prolonged drawdown phase followed by a partial recovery, while also showing that the observed rebound in the later years continues to remain much larger than that prediction obtained by the prior ensemble mean.

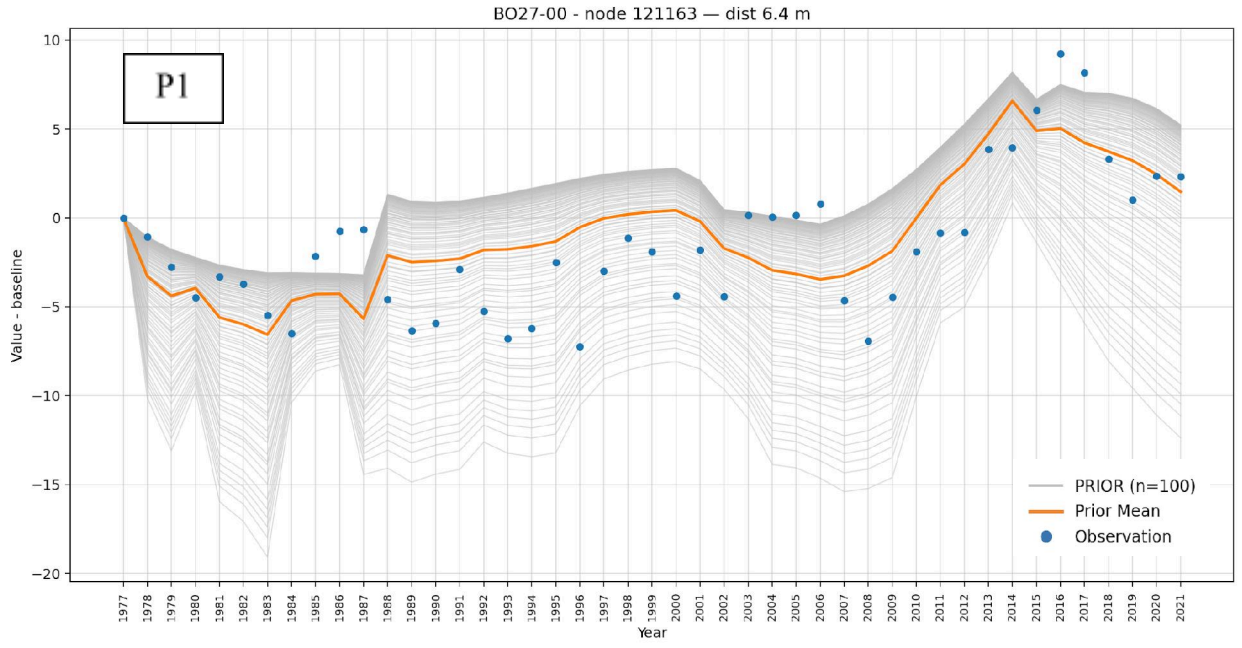

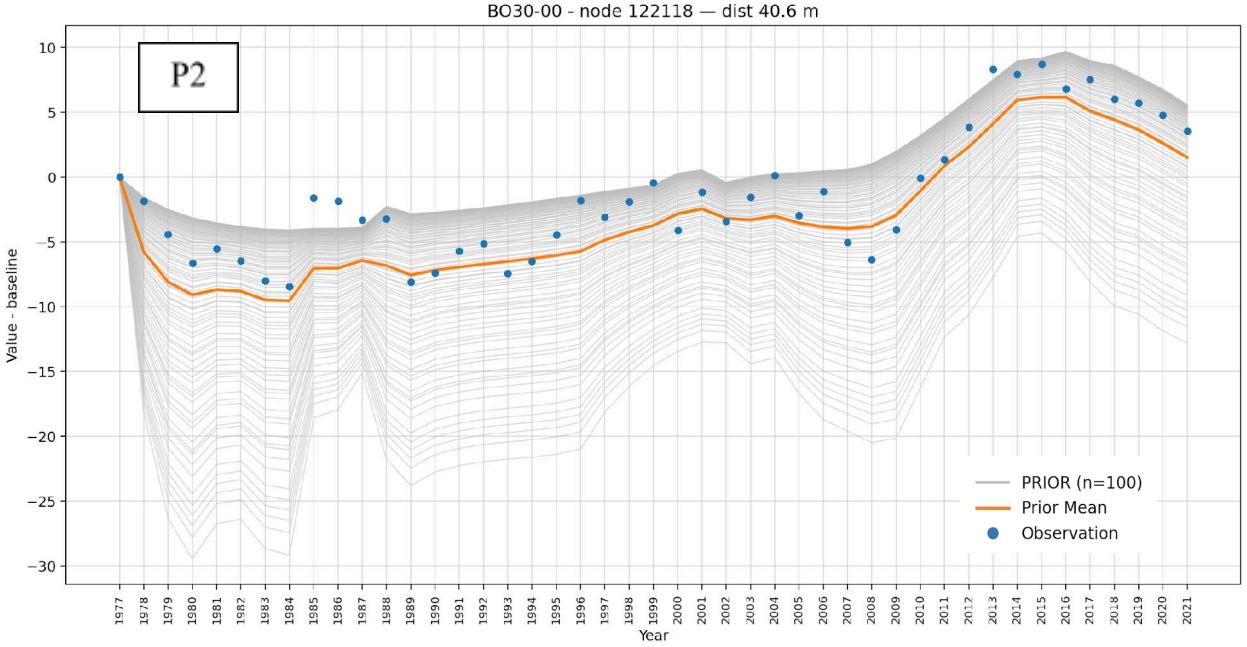
BO30-00 - node 122118 — dist 40.6 m
P2
Value - baseline
Year
PRIOR (n=100)
Prior Mean
Observation

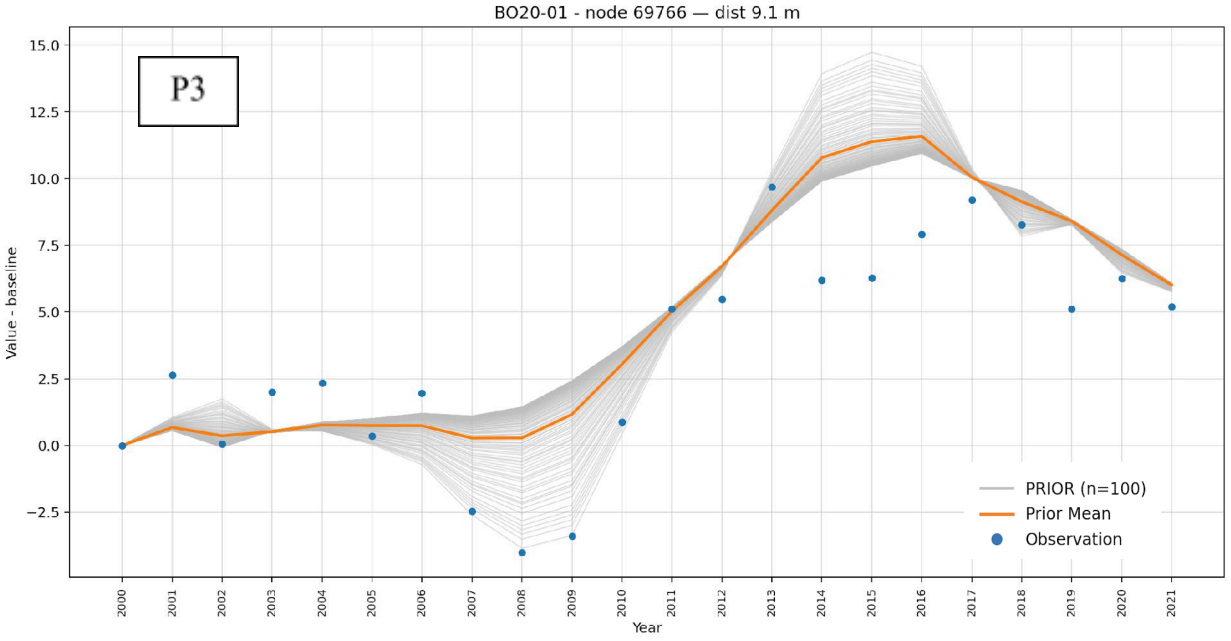
BO20-01 - node 69766 — dist 9.1 m
P3
Value - baseline
Year
PRIOR (n=100)
Prior Mean
Observation

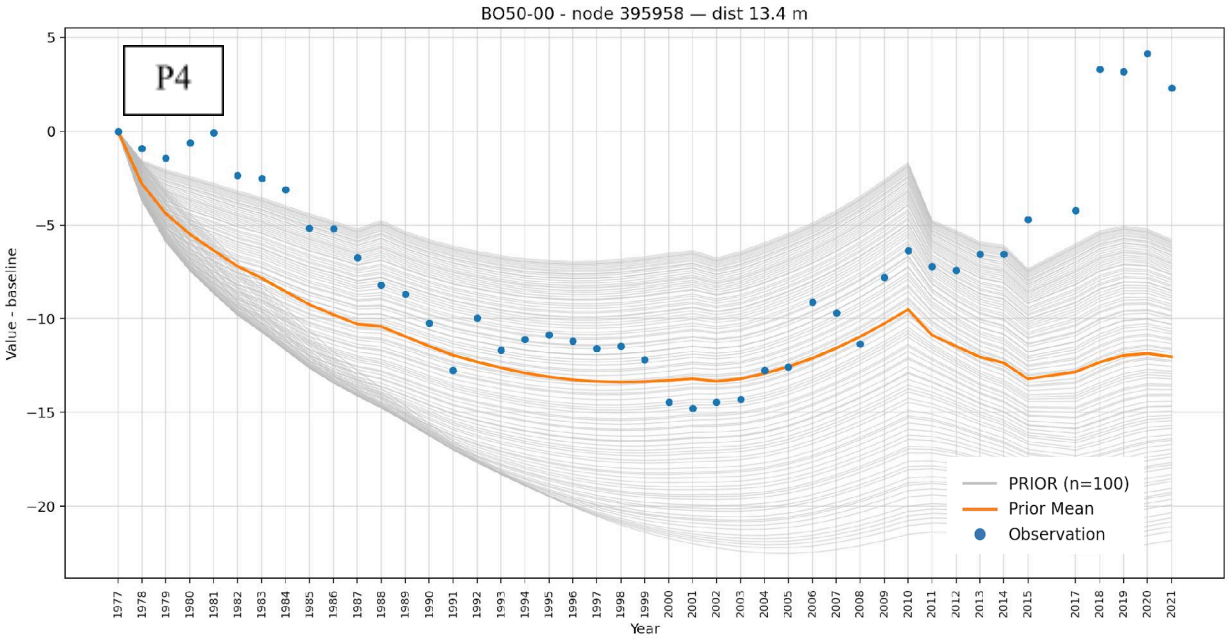

Figure 18 - Temporal evolution of hydraulic-head variations at the four representative pumping stations P1–P4, expressed as relative differences with respect to the first available observation year at each location. The observations are reported together with the prior ensemble obtained by SAT3D and the mean

4.1.2. Assimilation outcome for SAT3D

Different strategies have been adopted to perform the data assimilation using ES-MDA. As reported above, the prior uncertainty in hydraulic conductivity was initially represented by assigning independent uniform distributions to gravel and sand. More specifically, the hydraulic conductivity of gravel and that of sand were sampled separately by Latin Hypercube Sampling (LHS) over two distinct parameter domains. In this first parameterization, ES-MDA was applied to update both lithofacies simultaneously.

As shown in Figure 19, this strategy produced two independent cumulative distribution functions, one for gravel and one for sand, each approximately linear in log-space, which confirms that both priors were sampled uniformly within their prescribed ranges. However, the assimilation results were not satisfactory. If both parameters were allowed to vary independently, the resulting posterior did not lead to a clear and stable improvement in model performance: both posterior distributions do not change significantly relative to the prior ones, especially the one related to sandy soil. This suggests a classical overfitting problem, i.e. the available piezometric observations (in the quite few available piezometers within the study area) were insufficient to constrain robustly the distribution of two lithofacies.

To overcome this limitation, the parameterization was simplified. Instead of updating gravel and sand independently, only the hydraulic conductivity of gravel was treated as an uncertain parameter to be assimilated, while the hydraulic conductivity of sand was defined as a dependent quantity, fixed at a value 100 times smaller than that of gravel. In other words, the sand conductivity was no longer sampled independently but was linked directly to the gravel conductivity through a

prescribed proportional relationship. This reformulation reduced the dimensionality of the inverse problem and imposed a physically consistent contrast between the two lithofacies. The median value for the gravel K_z results equal to 20 m/day.

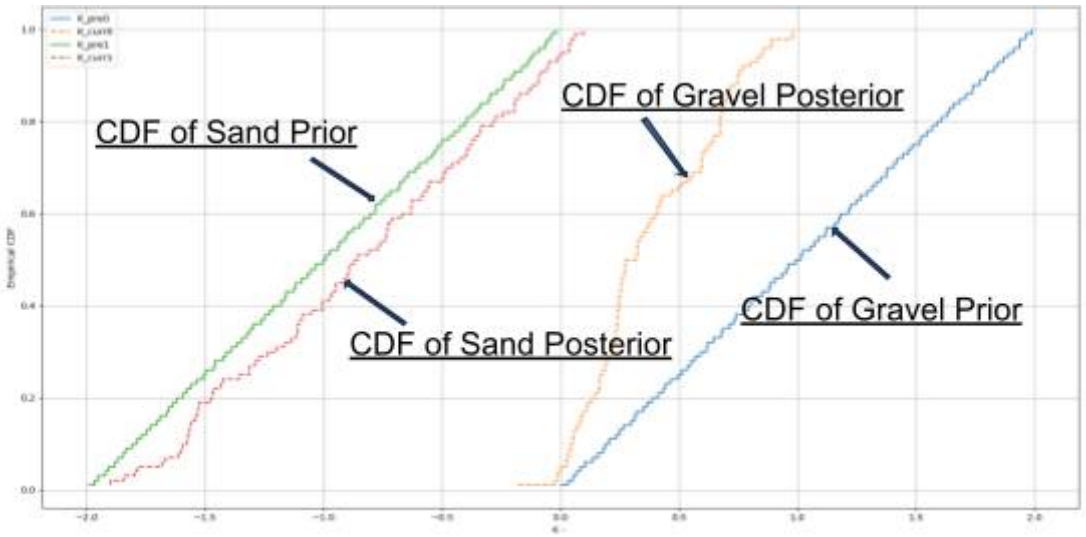

Figure 19 – Prior and posterior cumulative distribution functions of the hydraulic conductivity values assigned independently to gravel and sand. The two lithofacies were sampled separately by LHS

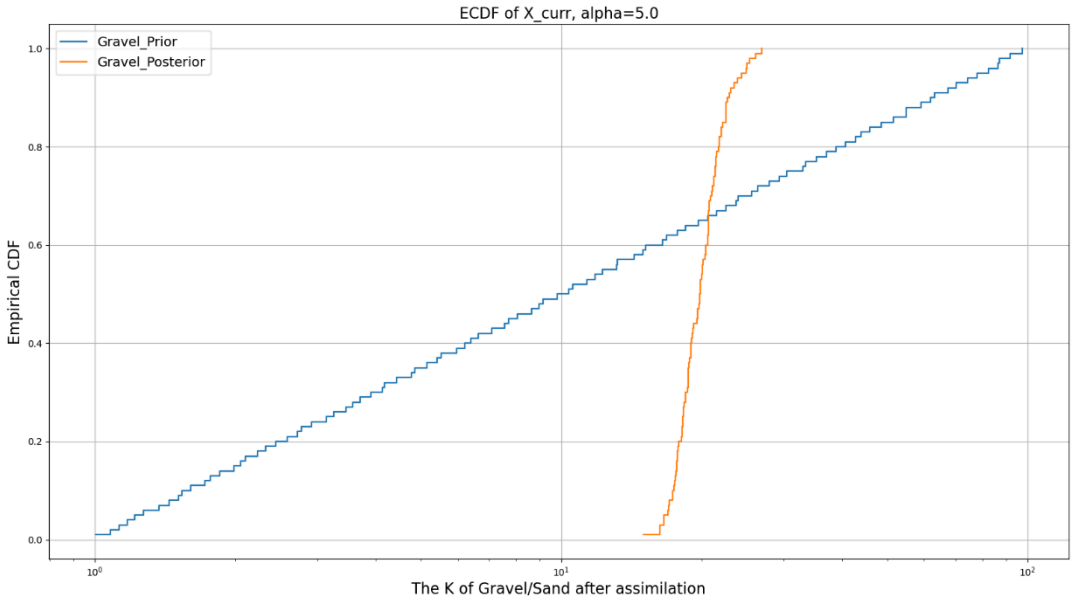

Figure 20 - Empirical cumulative distribution functions of the gravel hydraulic conductivity before and after ES-MDA assimilation under the revised parameterization

Under this revised setup, the ES-MDA results improved significantly. As illustrated by the posterior empirical cumulative distribution function in Figure 20, the updated gravel conductivity values are much more concentrated than in the prior distribution, indicating substantial uncertainty reduction

and clearer identification of the parameter range favored by the observations. This behaviour suggests that the assimilation process gains stability and effectiveness when the number of free hydraulic parameters is reduced and the hydraulic contrast between gravel and sand is enforced explicitly. Therefore, for the present case study, using a single assimilated gravel conductivity, with sand conductivity prescribed as two orders of magnitude lower, provides a more robust and successful ES-MDA calibration strategy than the initial approach based on two independently generated priors.

Figure 21 shows the temporal evolution of the simulated hydraulic-head variations at the four representative pumping stations, P1 to P4, before and after the ES-MDA assimilation. The green curves represent the posterior ensemble, while the red line denotes the posterior ensemble mean. Compared with the prior simulations, the posterior ensemble is visibly more compact at all four locations, indicating that the spread of the simulated responses has been reduced after assimilation.

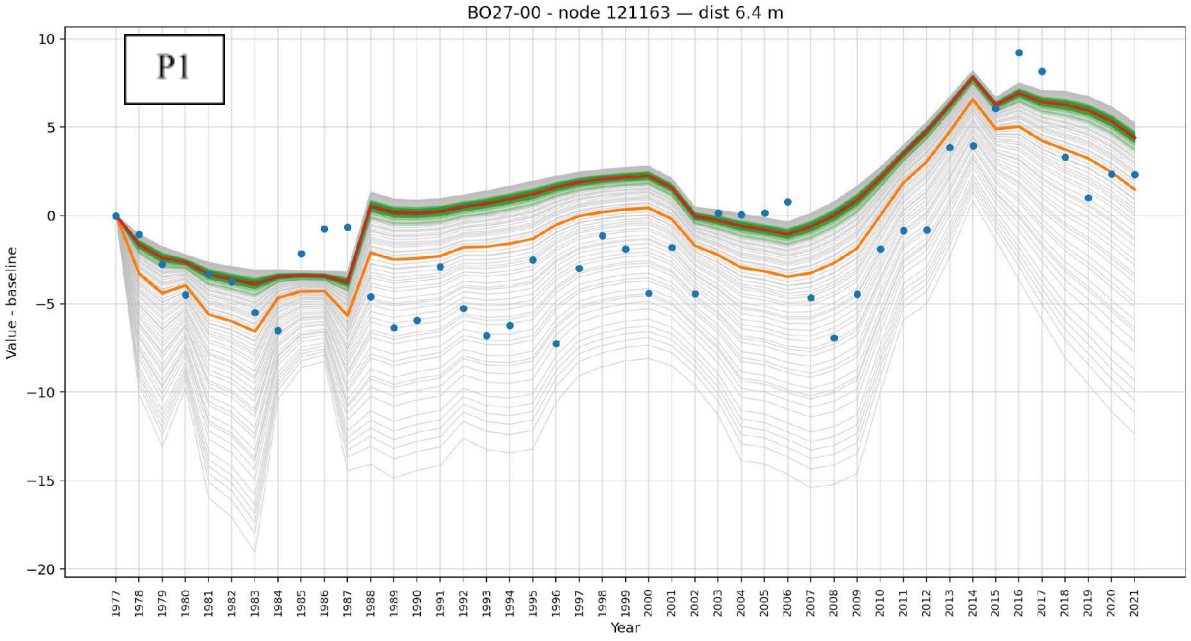

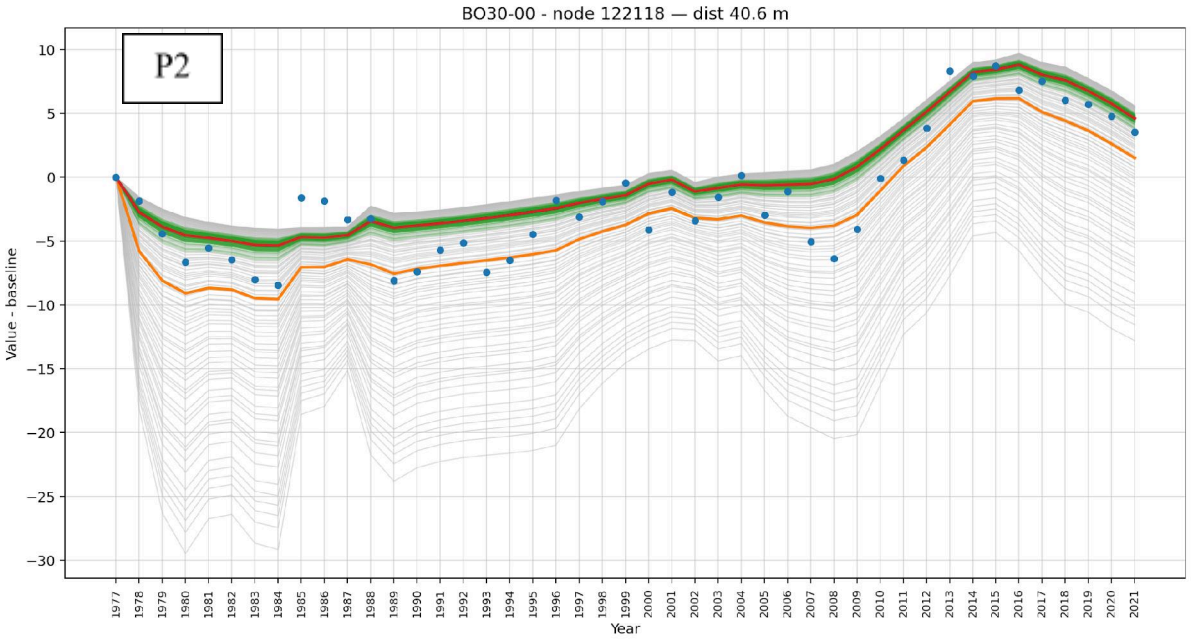
BO30-00 - node 122118 — dist 40.6 m
P2
Value - baseline
Year

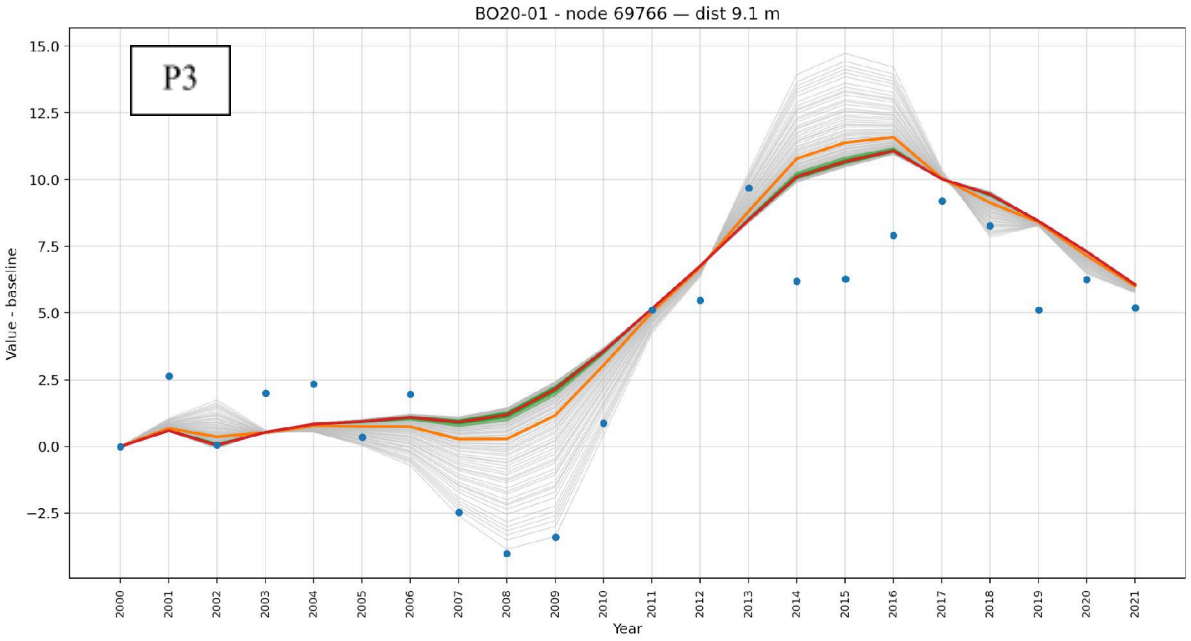
BO20-01 - node 69766 — dist 9.1 m
P3
Value - baseline
Year

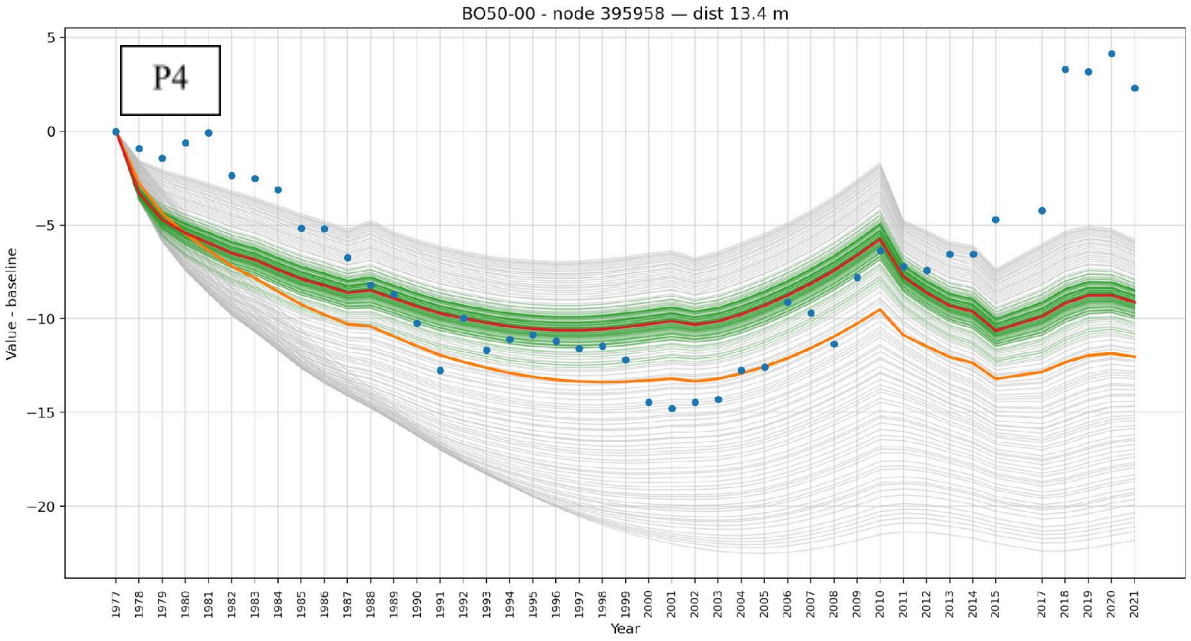

Figure 21 - Comparison between prior and posterior ensembles of hydraulic-head variations at the four representative pumping stations P1–P4, expressed as relative differences with respect to the first available observation year at each location

4.2. Land subsidence evolution

4.2.1. Initial tests using SUB3D and prior ensemble

In the case of the geomechanical model, the procedure adopted to generate the 100 prior realizations of compressibility is similar to that used for the groundwater flow model. However, in this stage of the analysis, the parameters selected for assimilation are the compressibilities of the clay and silty clay lithofacies. Initially, 100 compressibility realizations were generated by means of the LHS method using also in this case uniform distribution. For clay, the compressibility values were sampled within the range from 5×10^{-7} to 5×10^{-6} Pa^{-1}. Taking advantage of the experience acquired with the flow model, the compressibility of silty clay was then defined as a dependent quantity equal to one-half of the clay compressibility. By contrast, the compressibility of gravel and sand were kept fixed across all 100 realizations; the following values were adopted: 5×10^{-7} Pa^{-1} and 7×10^{-7} Pa^{-1}, respectively.

Figure 22 shows the temporal evolution of the simulated subsidence rate at the four representative locations P1–P4, which correspond to the same monitoring sites adopted in the groundwater-flow analysis. In each panel, the grey curves represent the 100 model realizations, the orange curve denotes the ensemble mean, and the blue dots indicate the observed deformation rates derived from InSAR data. The comparison illustrates both the spread of the prior geomechanical predictions and their behavior relative to the observed ground-motion rates at the selected locations over the period 1992–2021.

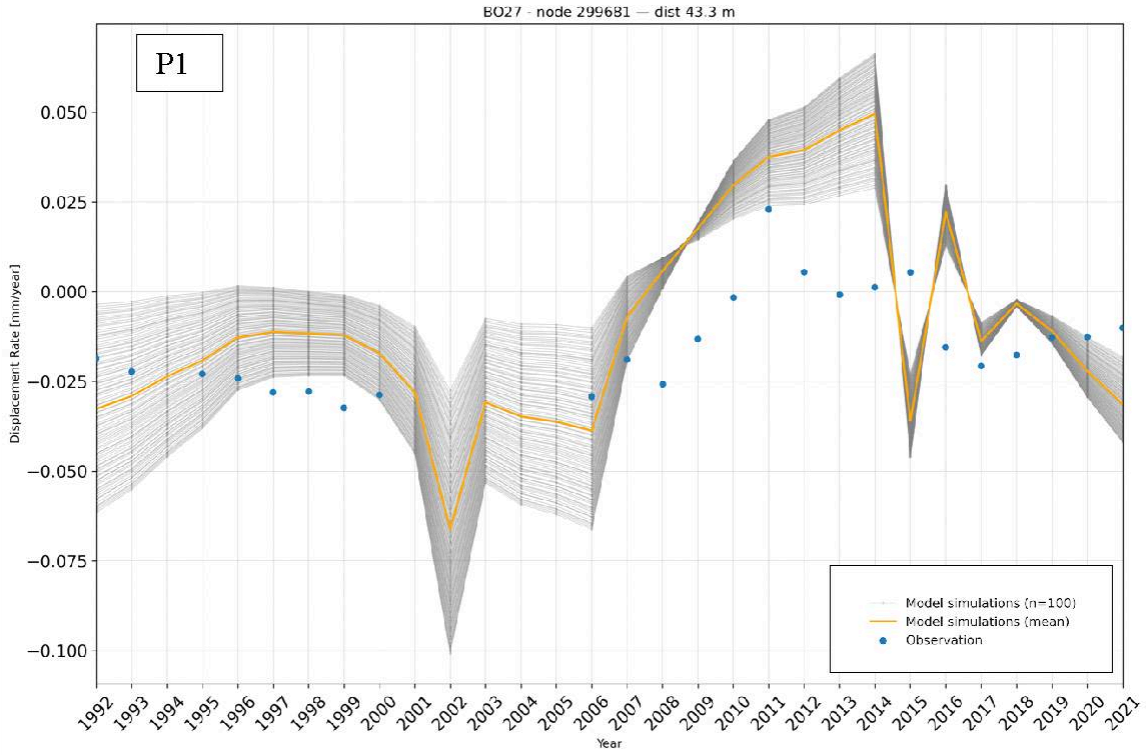
BO27 - node 299681 — dist 43.3 m
P1
Displacement Rate [mm/year]
Year
Model simulations (n=100)
Model simulations (mean)
Observation

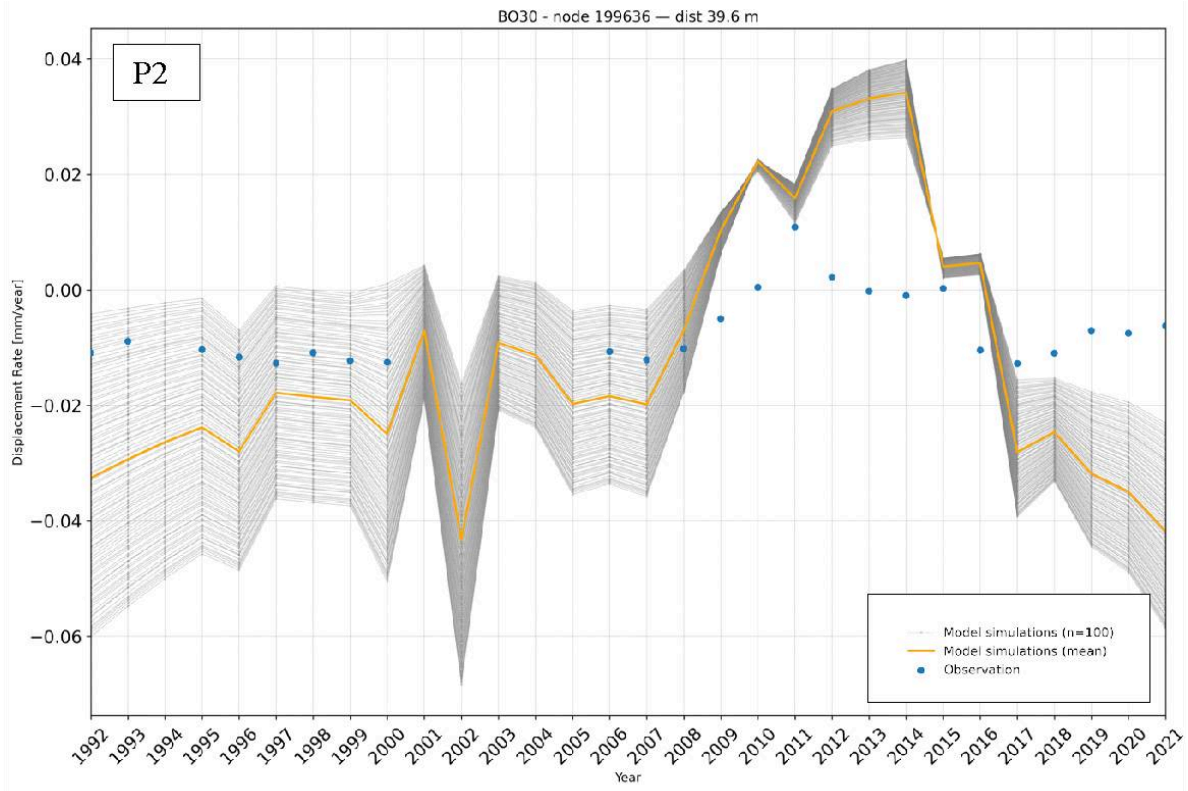
BO30 - node 199636 — dist 39.6 m
P2
Displacement Rate [mm/year]
Year
Model simulations (n=100)
Model simulations (mean)
Observation

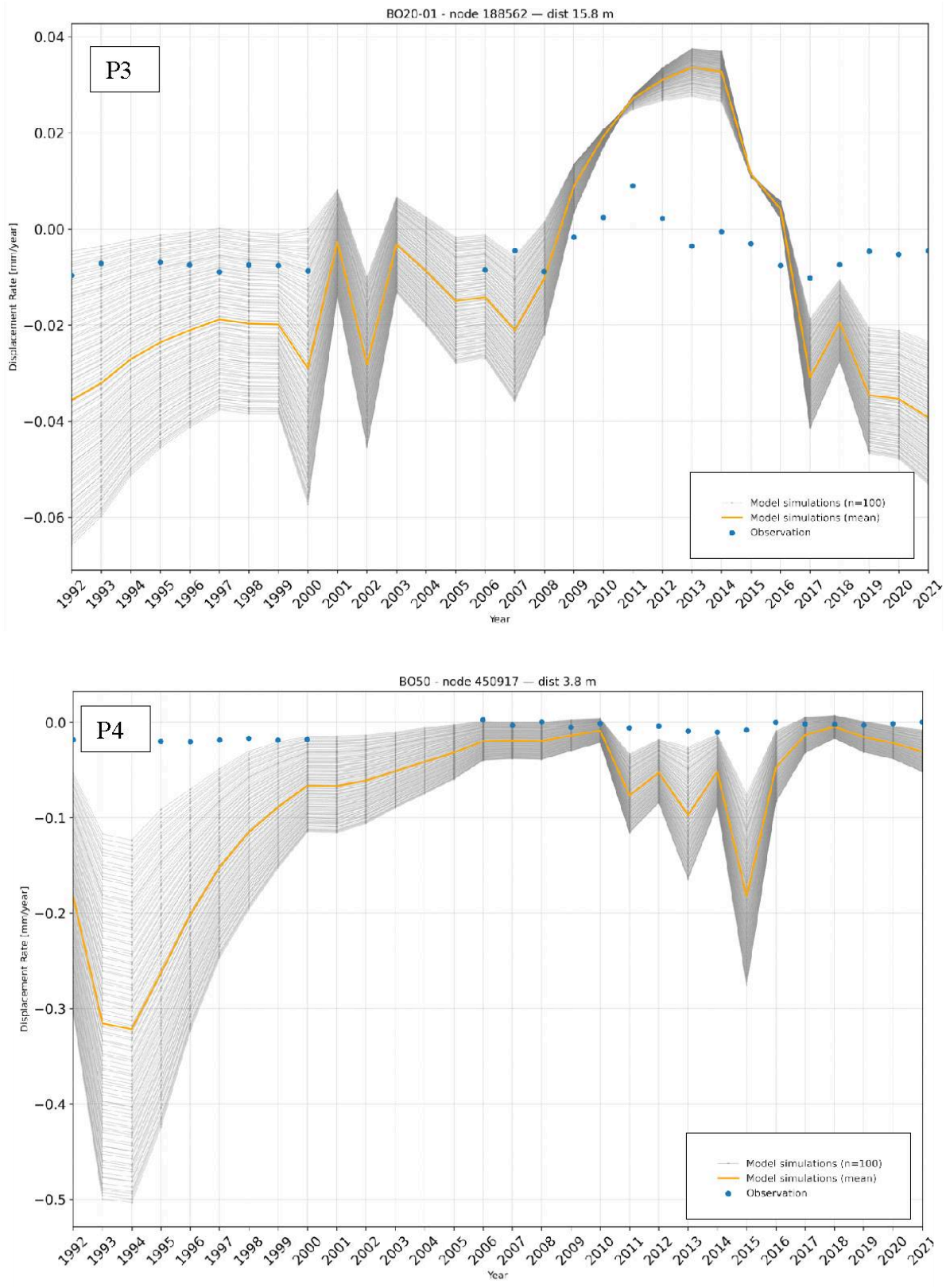

Figure 22 - Temporal evolution of the yearly subsidence rate at the four representative locations P1–P4, corresponding to the same sites used in the groundwater-flow analysis, for the period 1992–2021 monitored by InSAR

4.2.2. Assimilation outcome for SUB3D

The assimilation procedure adopted for the geomechanical model is analogous to that applied to the groundwater flow model. In the present case, the ES-MDA scheme is performed using a total of five iterative assimilation steps. This configuration allows the assimilation to proceed in a more stable and controlled manner, thereby reducing the risk of overcorrection. The observation-error covariance associated with the deformation data is set equal to 2 mm, which defines the uncertainty level assigned to the observed ground-motion measurements during the update process.

Figure 23 shows the cumulative distribution functions of the prior and posterior compressibility values before and after assimilation. The prior distribution spans a relatively wide range, reflecting the initial uncertainty assigned to the compressibility parameter. By contrast, the posterior distribution is markedly narrower and concentrated within a much smaller interval characterized by a median value equal to 1.2×10^{-6} Pa^{-1}. This result indicates that the assimilation of the observed deformation data has substantially reduced the uncertainty in the compressibility values. In other words, after assimilation, the admissible range of compressibility compatible with the observations becomes much more constrained than in the prior stage, demonstrating the effectiveness of the ES-MDA procedure in calibrating the geomechanical model.

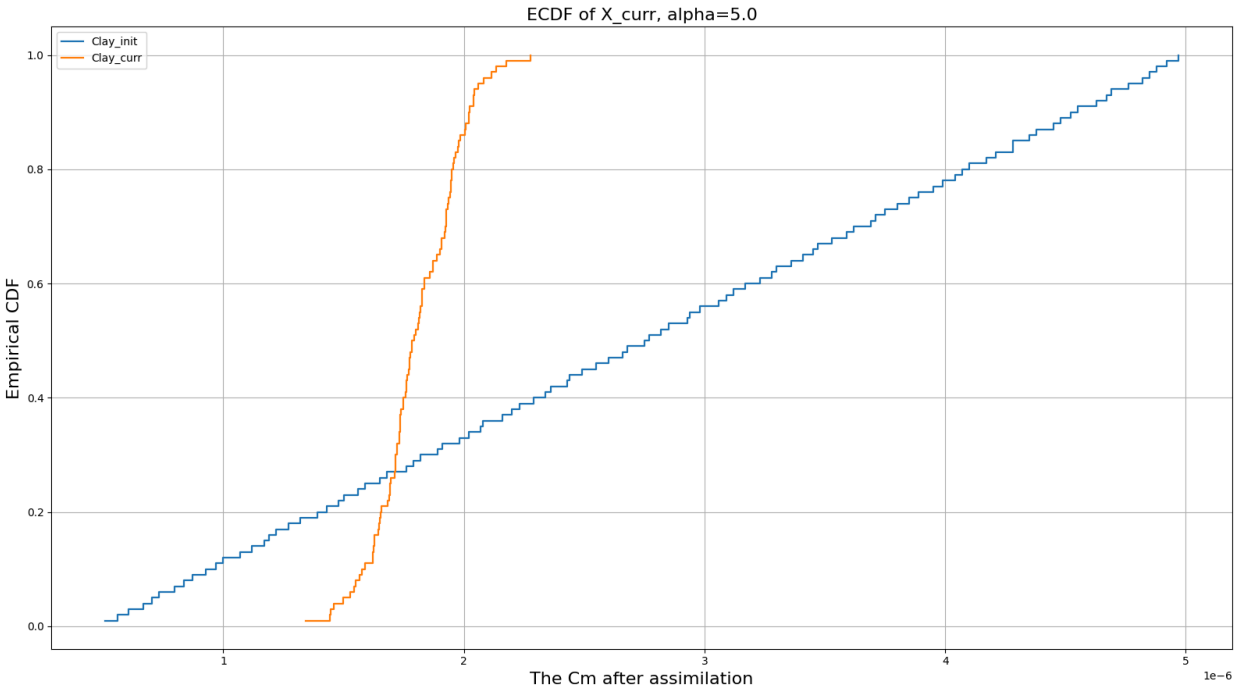

Figure 23 - Empirical cumulative distribution functions of the prior and posterior compressibility values for the clay lithofacies as used in the geomechanical model

Figure 24 shows the results obtained by rerunning the geomechanical model using the posterior compressibility ensemble derived from the ES-MDA procedure. In each panel, grey curves represent the prior simulations, light-blue curves represent the posterior simulations, the orange line denotes the prior mean, the blue line denotes the posterior mean, and red dots correspond to the observed deformation rates. Overall, the posterior parameter set leads to clear performance improvement at all four representative locations, as demonstrated by closer agreement between the posterior mean and observations and systematic RMSE reduction of up to 40%. Simultaneously, the

posterior ensemble is generally narrower than the prior one, indicating reduced uncertainty in the compressibility parameters after assimilation.

At P1, the posterior simulation provides substantial improvement. The posterior mean follows the observed temporal evolution more closely, especially from the early 1990s to the late 2000s, when the prior mean overestimates the amplitude of both subsidence and uplift. RMSE decreases from 24.5 mm to 14.6 mm (a 9.9 mm improvement). Although some mismatch remains during periods of stronger uplift, the posterior response is clearly more consistent with observations.

At P2, the improvement is even more pronounced. The posterior mean reproduces measured deformation rates much better over most of the investigated period. Notably, the excessive positive deformation predicted by the prior model around 2010–2015 is significantly reduced, and later-year behavior is better aligned with observed trends. RMSE decreases from 19.3 mm to 7.1 mm (a 12.2 mm improvement), indicating that updated compressibility values substantially enhance predictive capability at this location.

At P3, marked improvement is also evident. The posterior mean is noticeably closer to observations throughout most of the time series, particularly during the earlier subsidence-dominated phase and later transition period. RMSE is reduced from 21.2 mm to 7.9 mm (a 13.3 mm improvement), suggesting that assimilated compressibility values are more consistent with the local deformation response observed by InSAR.

At P4, despite exhibiting the largest residual mismatch among the four sites, the posterior simulation shows the greatest absolute improvement. In the prior model, simulated deformation rates are strongly overestimated in magnitude, especially during early years when predicted subsidence far exceeds observed values. After applying posterior parameters, this discrepancy is reduced, and the posterior mean moves closer to observations over the entire time interval. However, remaining mismatch indicates that local response at P4 is still difficult to reproduce accurately, likely due to stronger local heterogeneity or limitations in the current parameterization.

Collectively, these results confirm that rerunning the geomechanical model with the posterior compressibility ensemble produces systematic improvement in simulated deformation rates. Reduced RMSE values at all four locations demonstrate that the assimilation process has effectively constrained the mechanical parameters governing compaction. Moreover, the narrower posterior ensemble indicates that the updated parameter set yields a more consistent and physically constrained deformation response. Although some discrepancies remain, particularly at P4, the posterior simulations demonstrate that the ES-MDA procedure has significantly enhanced the geomechanical model's capability to reproduce observed subsidence-rate evolution.

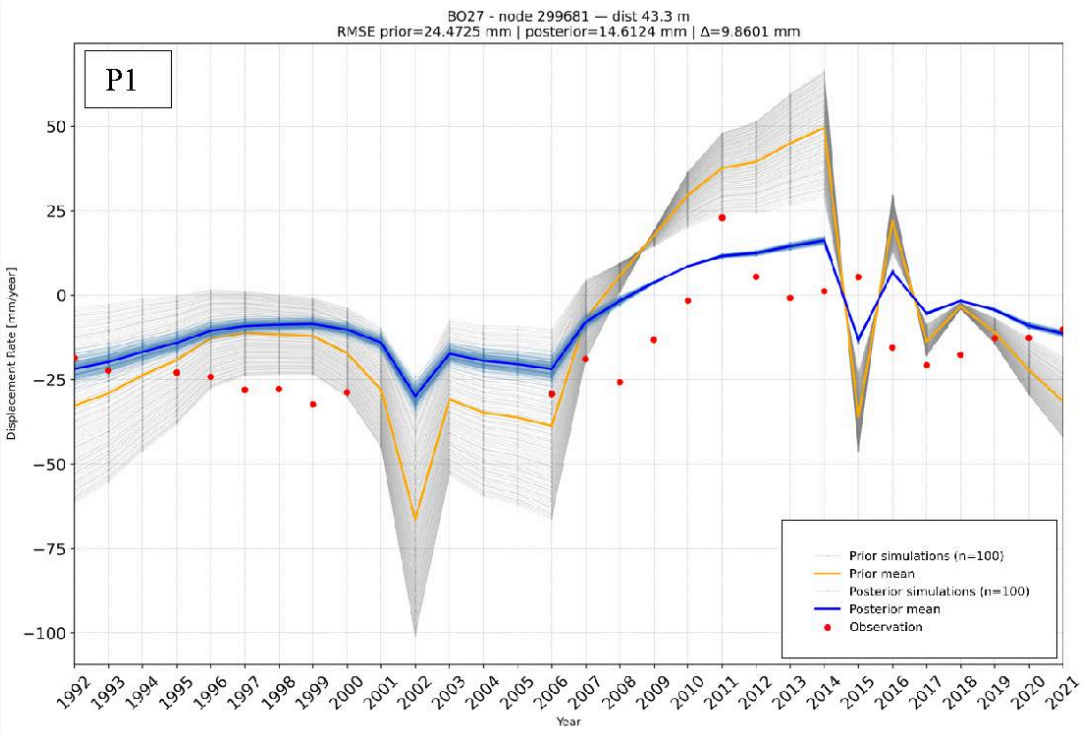
BO27 - node 299681 — dist 43.3 m
RMSE prior=24.4725 mm | posterior=14.6124 mm | Δ=9.8601 mm
P1
Displacement rate [mm/year]
Year
Prior simulations (n=100)
Prior mean
Posterior simulations (n=100)
Posterior mean
Observation

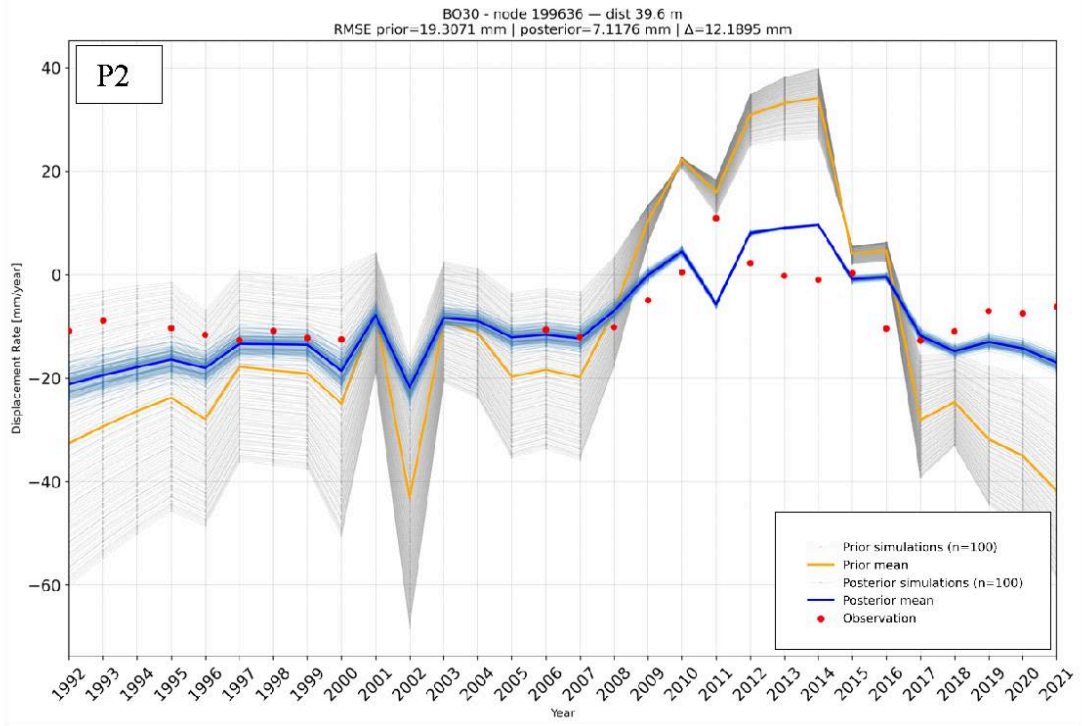
BO30 - node 199636 — dist 39.6 m
RMSE prior=19.3071 mm | posterior=7.1176 mm | Δ=12.1895 mm
P2
Displacement Rate [mm/year]
Year
Prior simulations (n=100)
Prior mean
Posterior simulations (n=100)
Posterior mean
Observation

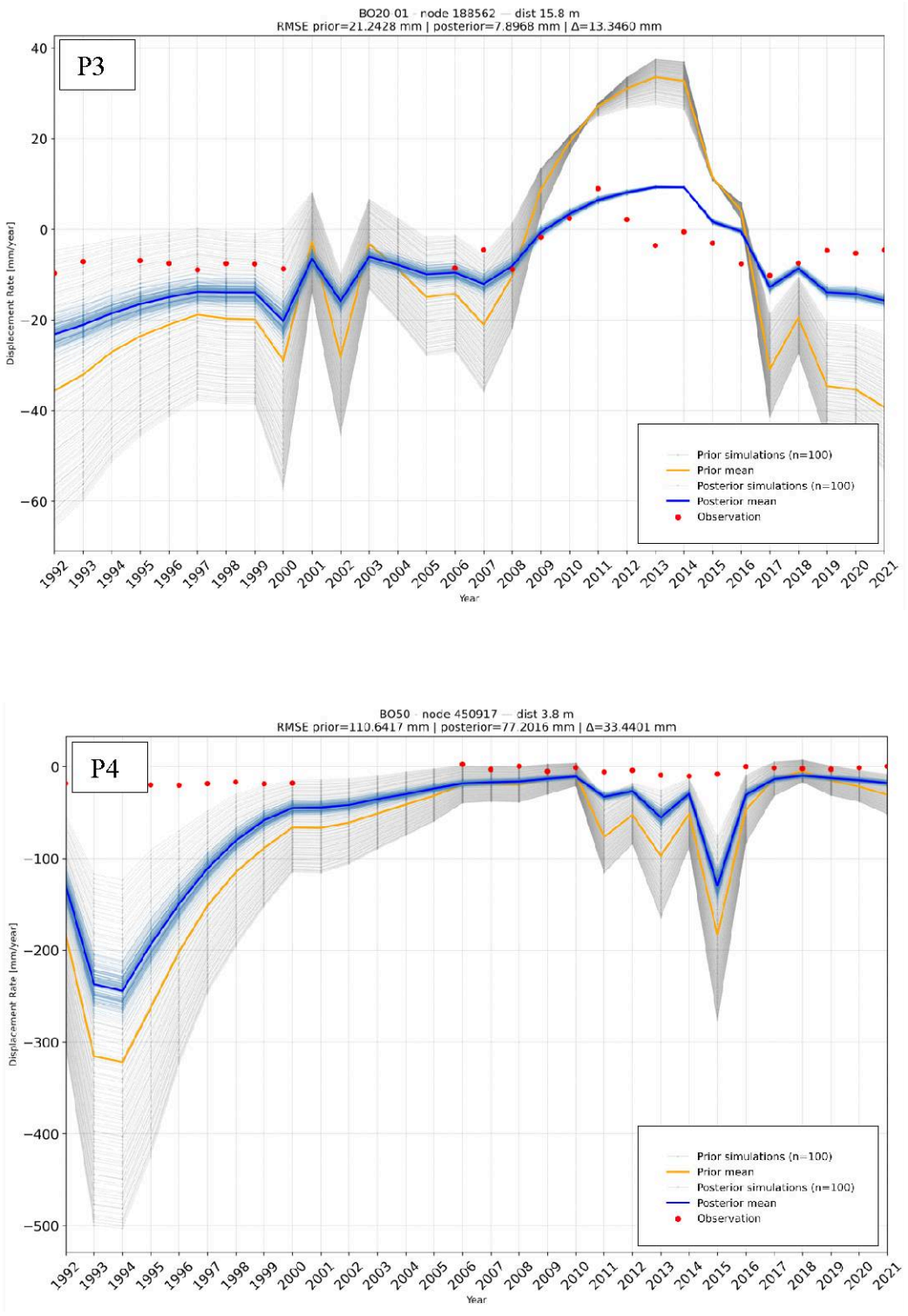

Figure 24 - Comparison between the prior and posterior results of the geomechanical model in terms of yearly rate of land subsidence at the four representative locations P1–P4 for the period 1992–2021. The InSAR records are provided

4.2.3. Maps of simulated land displacement rates in 2021

The maps of vertical displacements, i.e. land subsidence, and horizontal displacements along the west-east and south-north directions as provided by SUB3D using the media posterior compressibility values are provided in Figure 25, Figure 26, and Figure 27, respectively. Land subsidence rate ranges from 0 to 12 mm/year; the horizontal components are much smaller, with absolute value smaller than 5 mm/year along both the west-east and south-north directions.

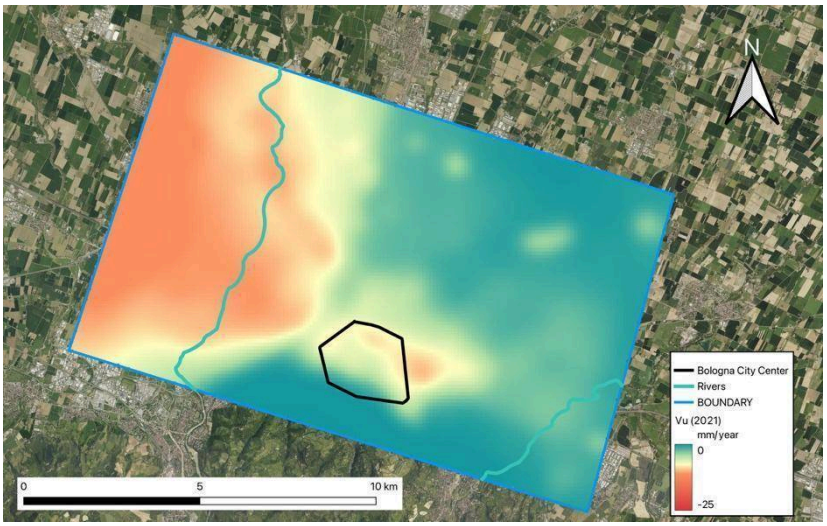

Figure 25 – Vertical displacement rate in 2021 as computed by SUB3D using the median posterior compressibility. Negative values mean land subsidence

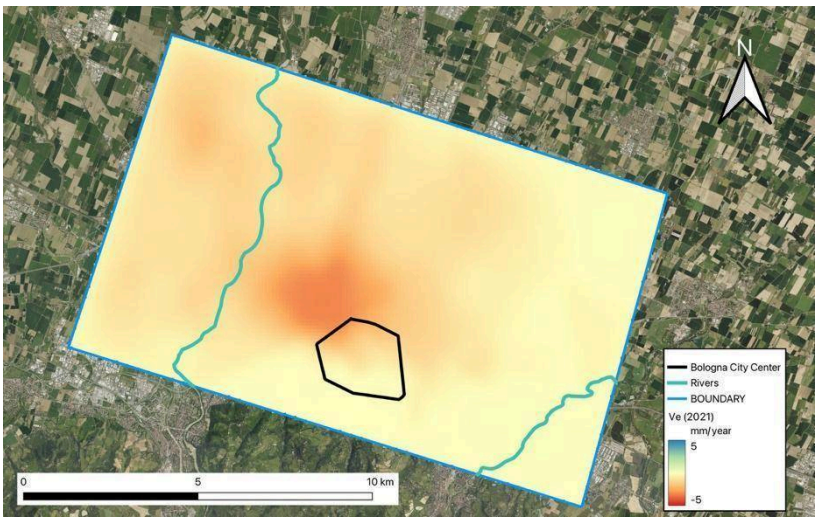

Figure 26 – West-east displacement rate in 2021 as computed by SUB3D using the median posterior compressibility. Positive values mean eastward displacements

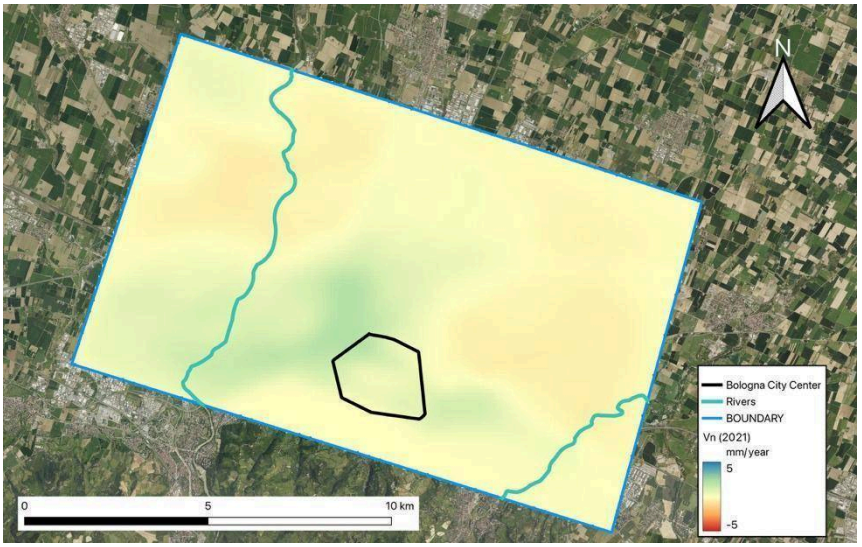

Figure 27 – South-north displacement rate in 2021 as computed by SUB3D using the median posterior compressibility. Positive values mean northward displacements

5. LAND SUBSIDENCE PREDICTION AT 2050 AND 2100

5.1. Input data: future population and precipitation

To predict the future evolution of hydraulic heads and, consequently, future land subsidence, it is essential to define plausible scenarios for both precipitation and population. These two variables represent key inputs for constructing the predictive framework, as they serve as reliable proxies for estimating future groundwater demand in terms of pumping rates and aquifer recharge to be assigned at the model boundaries.

Figure 28 shows population density in the metropolitan area of Bologna for the reference year 2020 and for the projected scenario in 2100. The maps were downloaded from the GHSL – Global Human Settlement Layer. According to this projection, the total population in the area is expected to decrease over the coming decades, reaching approximately 65% of the 2020 population by 2100. In other words, the projected reduction amounts to about 35% relative to present-day conditions. Based on this assumption, it has been assumed that the civil water consumption in 2100 will be likewise characterized by a same decrease of its 2021 value. A liner reduction between 2021 and 2100 has been assumed. This reduction is then used in the model to estimate future groundwater withdrawal associated with municipal demand.

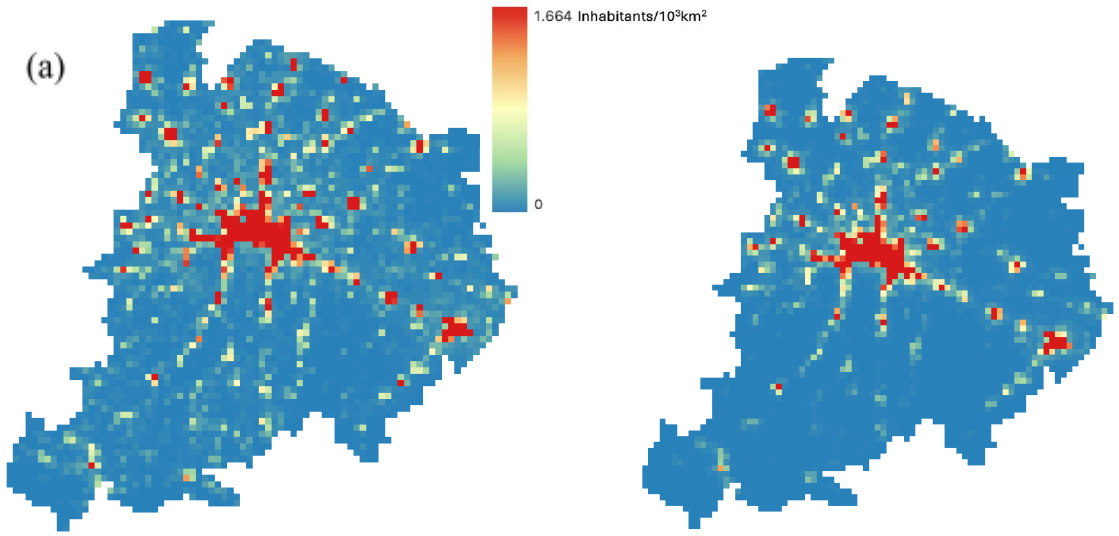

Figure 28 – Population density map in the Bologna metropolitan area in (a) 2020 and (b) 2100 as derived from GHSL – Global Human Settlement Layer (1 km) data.

Figure 29 presents annual mean precipitation time series under the RCP8.5 and RCP4.5 climate scenarios for the period 2006–2100. The scattered points represent yearly precipitation values retrieved by EURO-CORDEX Regional Climate Models (RCMs) and which underwent a bias-correction procedure as detailed in DEL6.3, while polynomial curves illustrate the overall long-term trends associated with each scenario. Both scenarios exhibit considerable interannual variability, with annual mean precipitation fluctuating over a relatively wide range throughout the simulation period, indicating that year-to-year precipitation remains highly variable regardless of

the emission scenario. However, when focusing on the smoothed trend lines rather than individual annual values, different long-term behaviors emerge.

Under the RCP8.5 scenario, the fitted curve shows a slight increase in annual mean precipitation during the first half of the century, followed by a gradual decline after approximately mid-century. This suggests that, although wetter years may still occur intermittently, the general tendency in later decades is toward reduced annual precipitation. By contrast, under the RCP4.5 scenario, the fitted curve remains comparatively stable over time, with only a modest increasing trend toward the end of the century. Overall, RCP4.5 maintains a more uniform precipitation regime than RCP8.5. Comparison between the two trend curves further indicates that divergence between scenarios becomes more evident in the second half of the century.

From a groundwater modeling perspective, precipitation is treated as an indirect control on aquifer system hydraulic conditions, primarily through its influence on groundwater recharge and, consequently, on regional hydraulic head distribution. Therefore, projected variations in precipitation under different climate scenarios are used as scaling factors to estimate future hydraulic boundary conditions of the numerical model.

Under the RCP4.5 scenario, the ratio between precipitation estimated for 2050 and that for 2021 is 0.98, indicating a slight 2% decrease by mid-century. The ratio between precipitation estimated for 2100 and that for 2050 is 1.05, corresponding to approximately 5% increase during the second half of the century. Assuming hydraulic conditions respond proportionally to these long-term changes in precipitation, the same scaling factors are applied to the hydraulic head field to estimate model boundary conditions for 2050 and 2100.

Under the RCP8.5 scenario, the ratio between precipitation estimated for 2050 and that for 2021 is 1.04, suggesting a moderate 4% increase by mid-century. Conversely, the ratio between precipitation estimated for 2100 and that for 2050 is 0.89, indicating approximately 11% decrease in the later part of the century. Following the same rationale adopted for RCP4.5, these ratios are also used as multiplicative factors to estimate the effective precipitation recharging the aquifer system and the future hydraulic head boundary conditions.

This assumption implies that long-term variation in boundary hydraulic heads is proportional to long-term variation in precipitation. Although this approach represents a simplification of actual recharge and flow processes, it provides a practical and physically consistent method for constructing future hydraulic boundary conditions in the absence of direct observations. In this way, the climate-driven influence of precipitation can be incorporated into predictive groundwater simulations, allowing the model to account for scenario-dependent changes in future hydraulic head evolution and, consequently, in the associated land subsidence response.

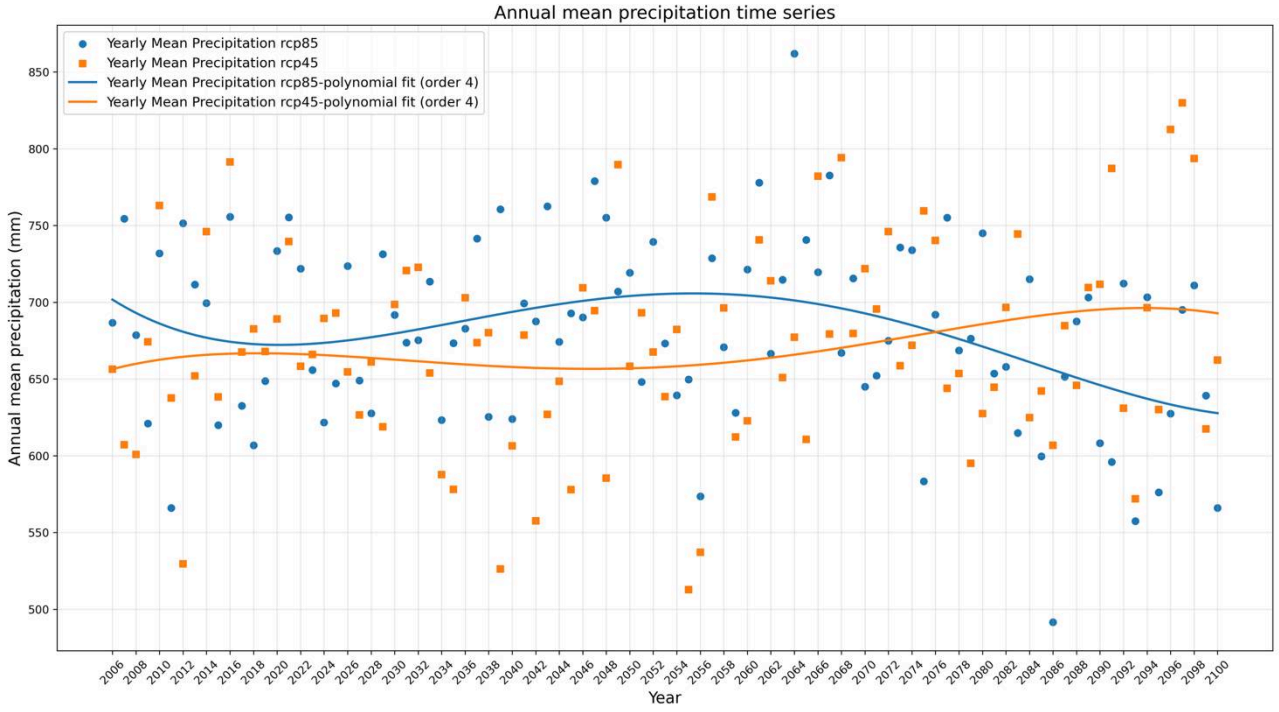

Figure 29 – Annual mean precipitation time series for the period 2006–2100 under the RCP4.5 and RCP8.5 climate scenarios retrieved from EURO-CORDEX RCMs and subjected to a bias-correction procedure (DEL6.3). The yearly values are fitted through a 3-order polynomial

5.2. Model forecast

The prediction phase from 2021 to 2100 has been carried out using the boundary conditions described above and the model parameters (i.e., hydraulic conductivity and compressibility) characterized by the values representing the median of the posterior distributions.

Figure 30 shows the simulated evolution of subsidence rates at the four representative locations P1–P4, combining the historical period up to 2021 with future projections from 2021 to 2100 under the RCP4.5 and RCP8.5 scenarios. In each panel, the orange line represents modeled subsidence rates during the historical period, whereas blue and green dashed lines represent projected future subsidence rates under RCP4.5 and RCP8.5, respectively.

For the future period, all curves indicate gradual reduction in subsidence magnitude, meaning that rates tend to become progressively less negative over time. At P1, P2, and P3, projected subsidence rates slowly approach values close to zero by the end of the century, suggesting a tendency toward stabilization of vertical ground movement under both climate scenarios. However, the two scenarios are not identical. After approximately mid-century, RCP4.5 projections provide a land subsidence decrease slightly faster than RCP8.5 projections, consistently with the precipitation trend. Collectively, the figure indicates that, according to model predictions, future land subsidence in the study area is expected to decrease in magnitude compared with the historical period, with ground-motion rates tending toward stabilization by 2100. Nevertheless, spatial differences remain important, and projected recovery is slightly faster under RCP4.5 than under RCP8.5.

The maps of displacement rate components at 2050 and 2100 for the two scenarios are shown in Figure 30 and Figure 31, respectively. The maps are also provided in digital version through DEL4.2 within SubRISK+ 'Control Room' (https://controlroom.subrisk.eu), for open visualization and browsing.

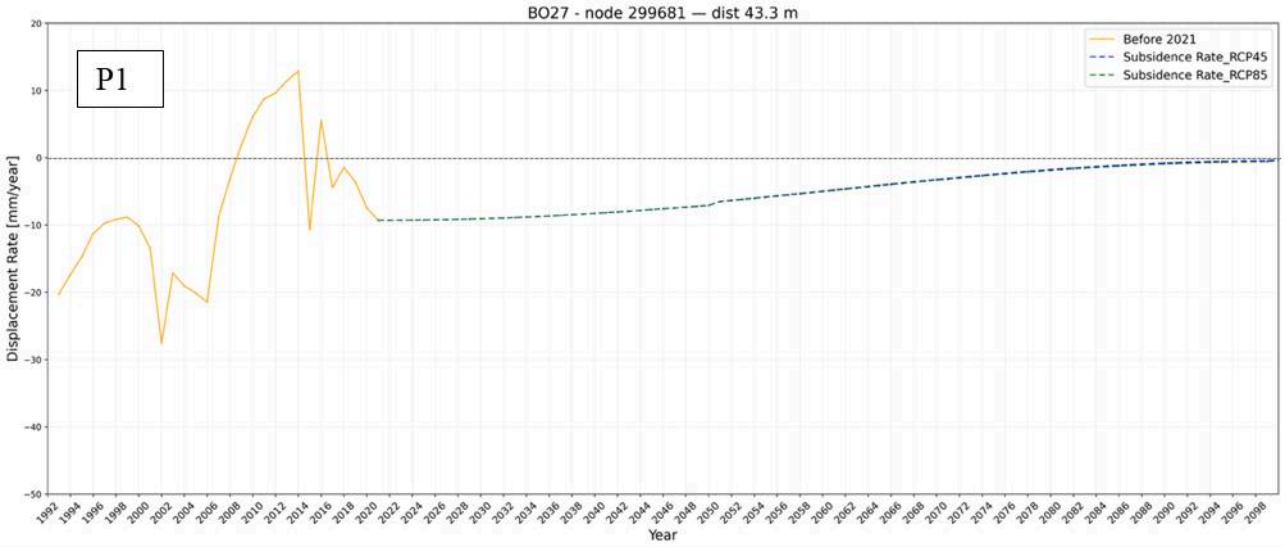

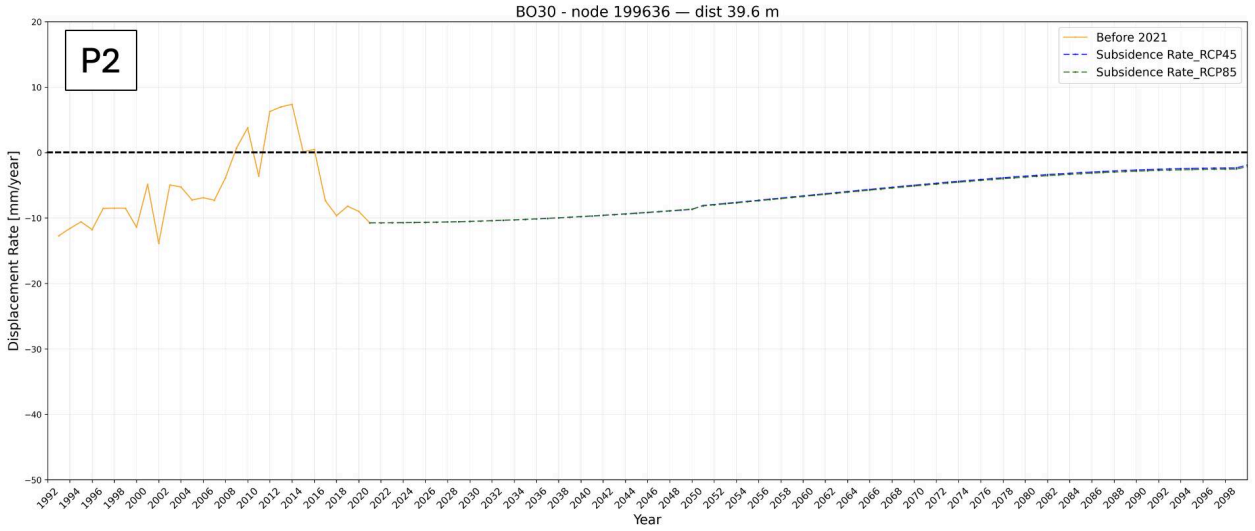

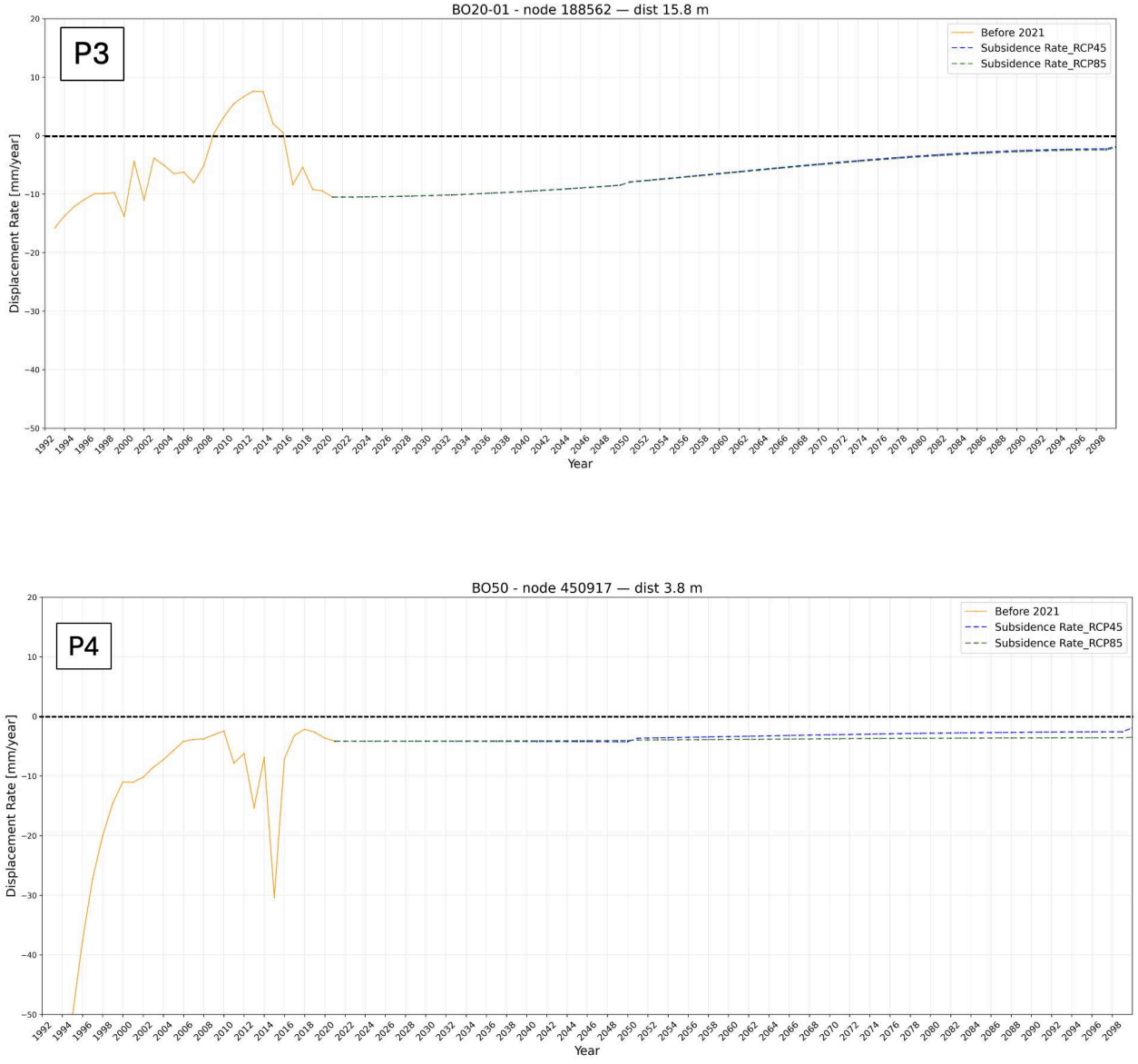

Figure 30 - Simulated subsidence-rate evolution at the four representative locations P1–P4, including the historical period up to 2021 and the future projections from 2021 to 2100 under the RCP45 and RCP85 scenarios

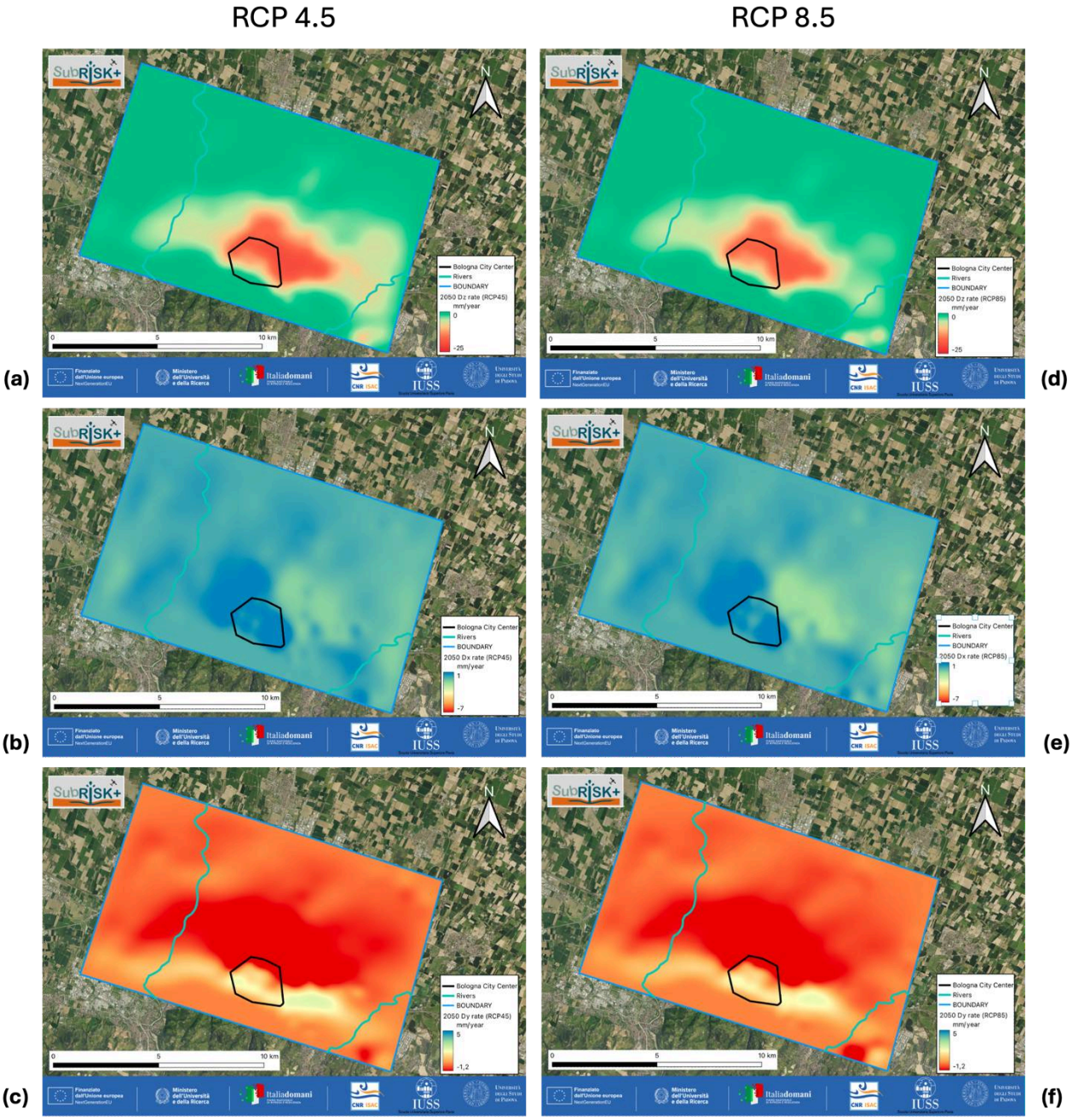

Figure 31 – Simulated (a,d) land subsidence rate, (b,e) west-east displacement rates, and (c,f) south-north displacement rates in 2050 with the RCP4.5 and RCP8.5 climatic scenarios, respectively

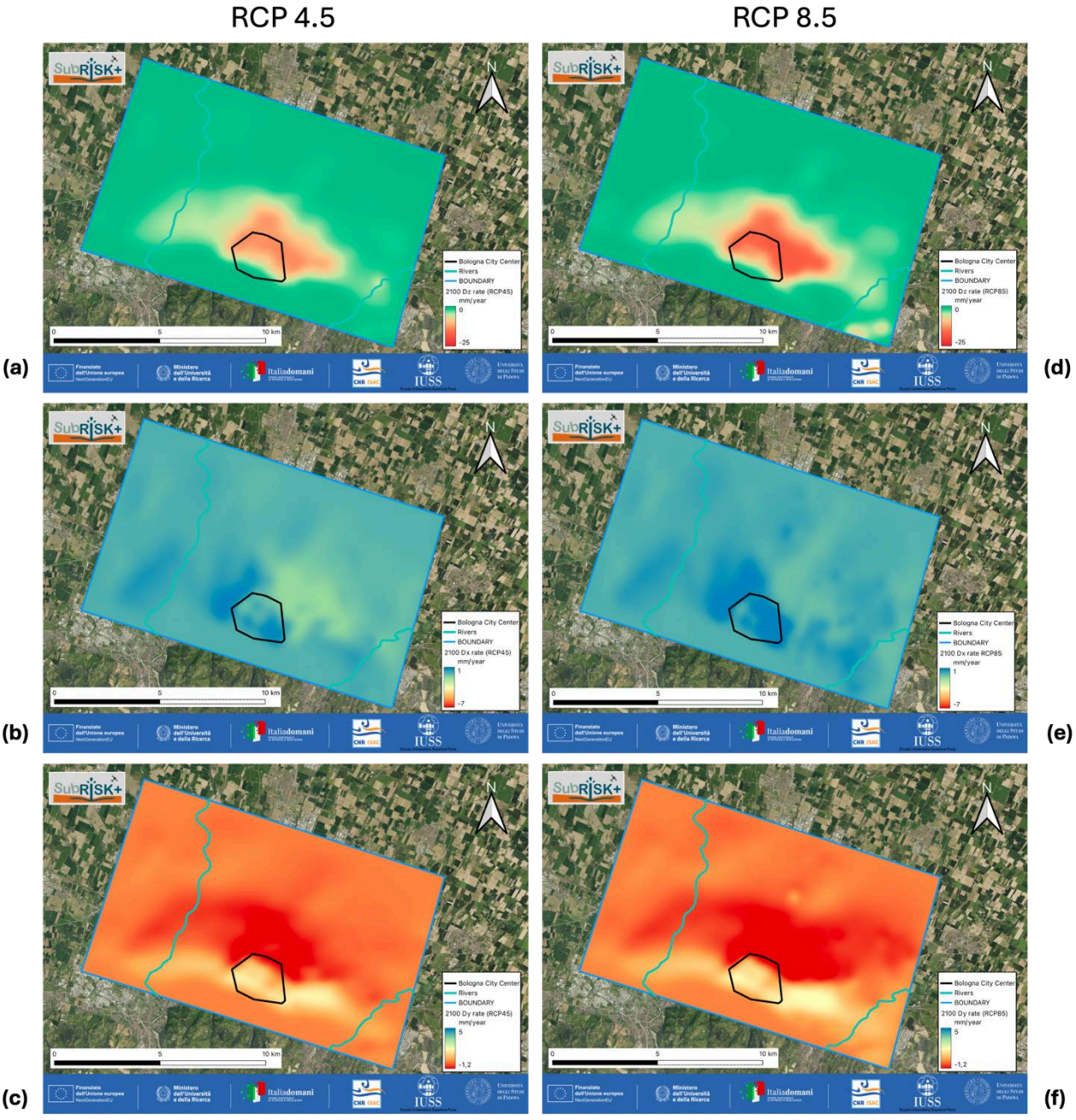

Figure 32 – Simulated (a,d) land subsidence rate, (b,e) west-east displacement rates, and (c,f) south-north displacement rates in 2100 with the RCP4.5 and RCP8.5 climatic scenarios, respectively

6. CONCLUSIONS

The present deliverable demonstrates the feasibility of applying the Ensemble Smoother with Multiple Data Assimilation (ES-MDA) to reduce parametric uncertainty in the hydro-geomechanical modelling of the Bologna aquifer system. It results particularly effective when direct information on layer properties is limited or incomplete. The results show that ES-MDA provides an effective framework for constraining key model parameters—such as hydraulic conductivity in the groundwater flow model and compressibility in the geomechanical model—by integrating numerical simulations with piezometric and InSAR observations. Since these parameters exert primary control on the accuracy of both the reconstructed historical response and predicted future evolution of hydraulic heads and land subsidence, their calibration represents a crucial step toward improving the reliability of the numerical modeling framework.

The assimilation results confirm that the methodology significantly reduces prior uncertainty and improves agreement between simulated and observed data. In the flow model, reduced uncertainty in hydraulic conductivity led to a narrower posterior ensemble and more consistent reproduction of hydraulic head variations at representative monitoring locations. In the geomechanical model, assimilation of deformation observations similarly reduced uncertainty in compressibility and improved the simulated subsidence-rate response, as demonstrated by systematic RMSE decrease after rerunning the model with the posterior parameter ensemble. These outcomes indicate that ES-MDA is not only computationally applicable in the present case study but also effective in producing physically meaningful posterior parameter ranges.

Simultaneously, the current analysis highlights an important limitation of the available observational system. Due to insufficient density and completeness of monitoring data, the model can presently constrain only a limited subset of lithofacies-dependent parameters rather than all material classes simultaneously. In practice, this means that the inverse problem must be simplified by prescribing physically consistent relationships among some lithofacies, so that only the most influential and observable parameters are updated. Although this limitation reduces the level of detail currently resolvable, it does not undermine the methodology's value. On the contrary, it demonstrates that ES-MDA can still be applied successfully under realistic data-scarce conditions, provided that parameterization is formulated in a physically consistent and parsimonious manner.

Overall, the present deliverable establishes a solid methodological basis for uncertainty reduction in the Bologna hydro-geomechanical model and confirms the potential of ES-MDA as a practical calibration tool for subsidence studies in multilayered aquifer systems. The calibrated posterior ensembles obtained in this work provide an improved starting point for future predictive simulations under different pumping and climate scenarios. Nevertheless, further progress depends on the availability of additional monitoring data, particularly data capable of constraining more lithofacies and improving spatial representativeness of both hydraulic and mechanical responses, for example records of different depth-interval compaction provided by extensometer stations. Future developments should therefore focus on expanding the observational dataset, refining the zonation and parameterization of lithological units, and extending the assimilation framework toward more comprehensive multi-parameter updating. In this way, the model's predictive capability for future hydraulic head evolution and land subsidence in the Bologna area can be further strengthened.

REFERENCES

Bear, J. 2013. *Dynamics of Fluids in Porous Media*. Courier Corporation.

Biot, Maurice A. 1941. 'General Theory of Three-Dimensional Consolidation'. *Journal of Applied Physics* 12(2): 155–64. doi:10.1063/1.1712886.

Emerick, A A., and A C. Reynolds. 2013. 'Ensemble Smoother with Multiple Data Assimilation'. *Computers & Geosciences* 55: 3–15. doi:10.1016/j.cageo.2012.03.011.

Gambolati, G., and R. A Freeze. 1973. 'Mathematical Simulation of the Subsidence of Venice: 1. Theory'. *Water Resources Research* 9(3): 721–33. doi:10.1029/WR009i003p00721.

Gambolati, G., P. Teatini, D. Baú, and M. Ferronato. 2000. 'Importance of Poroelastic Coupling in Dynamically Active Aquifers of the Po River Basin, Italy'. *Water Resources Research* 36(9): 2443–59. doi:10.1029/2000wr900127.

Ochoa-Gonzalez, G. H., D. Carreon-Freyre, A. Franceschini, M. Cerca, and P. Teatini. 2018. 'Overexploitation of groundwater resources in the faulted basin of Queretaro, Mexico: a 3D deformation and stress analysis'. *Engineering Geology*, 245, 192-206.

Teatini, P., G. Gambolati and L. Tosi. 1995. 'A new 3-D non-linear model of the subsidence of Venice'. In: *Land Subsidence, Proc. 5th Int. Symp. on Land Subsidence*, F.B.J. Barends et al. eds., IAHS Publ. NO. 234, UK, 353-361.

Teatini, P., M. Ferronato, G. Gambolati, and M. Gonella. 2006. 'Groundwater Pumping and Land Subsidence in the Emilia‐Romagna Coastland, Italy: Modeling the Past Occurrence and the Future Trend'. *Water Resources Research* 42(1). doi:10.1029/2005wr004242.

Teatini, P., G. Gambolati, M. Ferronato, A. Settari and D. Walters. 2011. 'Land uplift due to subsurface fluid injection'. *J. of Geodynamic*s, 51(1), 1-16. doi:10.1016/j.jog.2010.06.001.

Verruijt, A. 1969. 'Elastic storage of aquifers'. *Flow through porous media.* R. De Wiest, ed., Academic Press, New York, 331–376

Zhu, L., A. Franceschini, H. Gong, M. Ferronato, Z. Dai, Y. Ke, Y. Pan, X. Li, R. Wang and P. Teatini. 2020. 'The 3-D facies and geomechanical modeling of land subsidence in the Chaobai Plain, Beijing'. *Water Resources Research*, 54, doi:10.1029/2019WR027026.

Zuccarini, A., S. Giacomelli, P. Severi, and M. Berti. 2024. 'Long-Term Spatiotemporal Evolution of Land Subsidence in the Urban Area of Bologna, Italy'. *Bulletin of Engineering Geology and the Environment* 83(1): 35. doi:10.1007/s10064-023-03517-5.